General Disclaimer

One or more of the Following Statements may affect this Document

- This document has been reproduced from the best copy furnished by the organizational source. It is being released in the interest of making available as much information as possible.

- This document may contain data, which exceeds the sheet parameters. It was furnished in this condition by the organizational source and is the best copy available.

- This document may contain tone-on-tone or color graphs, charts and/or pictures, which have been reproduced in black and white.

- This document is paginated as submitted by the original source.

- Portions of this document are not fully legible due to the historical nature of some of the material. However, it is the best reproduction available from the original submission.

NASA TECHNICAL NOTE

NASA TN D-8292

A SPECTRAL REFLECTANCE ESTIMATION
TECHNIQUE USING MULTISPECTRAL DATA
FROM THE VIKING LANDER CAMERA

Stephen K. Park and Friedrich O. Huck

Langley Research Center
Hampton, Va. 23665

NATIONAL AERONAUTICS AND SPACE ADMINISTRATION • WASHINGTON, D. C. • NOVEMBER 1976

1. Report No. NASA TN D-8292	2. Government Accession No.	3. Recipient's Catalog No.
4. Title and Subtitle A SPECTRAL REFLECTANCE ESTIMATION TECHNIQUE USING MULTISPECTRAL DATA FROM THE VIKING LANDER CAMERA		5. Report Date November 1976
		6. Performing Organization Code
7. Author(s) Stephen K. Park and Friedrich O. Huck		8. Performing Organization Report No. L-10681
9. Performing Organization Name and Address NASA Langley Research Center Hampton, VA 23665		10. Work Unit No. 506-25-99-00
		11. Contract or Grant No.
12. Sponsoring Agency Name and Address National Aeronautics and Space Administration Washington, DC 23665		13. Type of Report and Period Covered Technical Note
		14. Sponsoring Agency Code

15. Supplementary Notes

16. Abstract

A technique is formulated for constructing spectral reflectance curve estimates from multispectral data obtained with the Viking lander camera. The multispectral data are limited to six spectral channels in the wavelength range from 0.4 to 1.1 μm, and most of these channels exhibit appreciable out-of-band response. The output of each channel is expressed as a linear (integral) function of the (known) solar irradiance, atmospheric trans-mittance, and camera spectral responsivity and the (unknown) spectral reflectance. This produces six equations which are used to determine the coefficients in a representation of the spectral reflectance as a linear combination of known basis functions. Natural cubic spline reflectance estimates are produced for a variety of materials that can be reasonably expected to occur on Mars. In each case the dominant reflectance features are accurately reproduced, but small period features are lost due to the limited number of channels. The results also suggest that this technique may be a valuable aid in selecting the number of spectral channels and their responsivity shapes when designing a multispectral imaging system.

17. Key Words (Suggested by Author(s)) Viking lander camera Multispectral-data analysis Spectral reflectance estimates	18. Distribution Statement Unclassified – Unlimited Subject Category 19		
19. Security Classif. (of this report) Unclassified	20. Security Classif. (of this page) Unclassified	21. No. of Pages 42	22 Price* $3.75

A SPECTRAL REFLECTANCE ESTIMATION TECHNIQUE
USING MULTISPECTRAL DATA FROM THE
VIKING LANDER CAMERA

Stephen K. Park and Friedrich O. Huck.
Langley Research Center

SUMMARY

A technique is formulated for constructing spectral reflectance curve estimates from multispectral data obtained with the Viking lander camera. The multispectral data are limited to six spectral channels in the wavelength range from 0.4 to 1.1 μm, and most of these channels exhibit appreciable out-of-band response. The output of each channel is expressed as a linear (integral) function of the (known) solar irradiance, atmospheric transmittance, and camera spectral responsivity and the (unknown) spectral reflectance. This produces six equations which are used to determine the coefficients in a representation of the spectral reflectance as a linear combination of known basis functions. The natural cubic spline basis functions generally produce the best estimates.

Reflectance estimates are produced for a variety of materials that can be reasonably expected to occur on Mars. In each case the dominant reflectance features are accurately reproduced, but small period features are lost due to the undersampling inherent with the limited number of channels. The results also suggest that the estimation technique may be a valuable aid in selecting the number of spectral channels and their responsivity shapes when designing a multispectral imaging system.

INTRODUCTION

The Viking lander cameras (refs. 1 and 2) will return multispectral images of the Martian surface with resolution higher by four orders of magnitude than has been previously obtained. It is desired to extract spectral reflectance curves from these data. However, the data are limited to six spectral channels, and most of these channels exhibit out-of-band response.

It is inappropriate to generate a data point for each channel by associating a reflectance value with a distinct wavelength; this is particularly true for those channels with appreciable out-of-band response. It is unlikely that data points so constructed will lie on the true reflectance curve and that any method of fitting a curve to these points will adequately approximate the true reflectance.

Instead, the output of each channel can be expressed as a linear (integral) function of the unknown spectral reflectance and of the known solar irradiance, atmospheric transmittance, and camera responsivity. This produces six equations which can be used to determine the coefficients in a representation of the spectral reflectance as a linear combination of known basis functions. Several sets of basis functions are discussed — polynomials and cubic splines — and their appropriateness is evaluated by constructing reflectance estimates for a variety of materials that can be reasonably expected to occur on the Martian surface and for the reference test charts that are located on each lander. The quality of these estimates is determined by comparison with the estimates that could be obtained by using an idealized camera response, represented by impulse functions, which provides an accurate reflectance sample at a distinct wavelength for each channel.

SYMBOLS

A 6×6 system matrix

A^{-1} inverse of A

$\underline{A}$ 8×8 matrix formed from A (see table II)

a_{ij} elements of matrix $\underline{A}$

b_i spectral sample for ith channel

$\underline{b}$ column vector with elements 0, b_1, b_2, . . ., b_6, 0

$C(\lambda)$ cubic spline basis function

$C''(\lambda)$ second derivative of $C(\lambda)$

c_i system calibration constant for ith channel, V

e_i measure of error (see eq. (10c))

$F(\lambda)$ relative standard deviation of reflectance estimate

$f_i(\lambda)$ system characteristic function

$h_j(\lambda)$ basis function

$\underline{h}(\lambda)$ column vector with elements $h_0(\lambda)$, $h_1(\lambda)$, . . ., $h_7(\lambda)$

n number of basis functions

$R_i(\lambda)$ channel responsivity, A/W

$S(\lambda)$ solar irradiance, kW/m^2-μm

$T_i(\lambda)$ system transfer function for ith channel, μm^{-1}

t_i scaling constant (see eqs. (5))

V_i channel voltage, V

V_i^r channel voltage corresponding to reference reflectance, V

x_j coefficient of basis function $h_j(\lambda)$

$\underline{x}$ column vector with elements x_0, x_1, x_2, . . ., x_6, x_7

Δ spacing between adjacent spline knots (0.12 μm)

$\delta(\lambda - \lambda_i)$ delta (impulse) function located at λ_i

$\epsilon(\lambda)$ estimate error (see eq. (8))

ι incidence angle, deg

λ wavelength, μm

λ_i location of impulse system transfer functions, μm

$\bar{\lambda}_j$ location of cubic spline knots, μm

$\rho(\lambda)$ actual spectral reflectance

$\rho_r(\lambda)$ actual spectral reflectance of reference test-chart patches

$\langle \rho(\lambda) \rangle$ estimated spectral reflectance

σ	standard deviation
σ_p	standard deviation of reflectance estimate
$\tau_a(\lambda)$	atmospheric transmittance
$\tau_c(\lambda)$	camera optical throughput
$(\ )^T$	transpose of $(\ )$

CAMERA SYSTEM

Description

Figure 1 shows a cutaway view of the Viking lander camera. Light that passes from the scene through the window is reflected by a scanning mirror to an objective lens which images this light onto a plane containing an array of photosensors, each covered by a small aperture that defines the instantaneous field of view. The photosensors convert the light into an electrical signal which is amplified, sampled, and quantized for digital transmission. The camera rotates a small step in azimuth between elevation line scans until the entire scene of interest is scanned. General design and performance characteristics are listed in table I.

The camera features an array of 12 silicon photodiodes, consisting of 4 broadband channels with selectable focus for high-resolution imaging, 1 broadband channel for low-resolution surveys, 6 narrowband channels for multispectral color and near-infrared imaging, and 1 narrowband red channel for scanning the Sun. Typical responsivities for the six narrowband channels are plotted in figure 2. The three spectral channels in the visual (0.4 to 0.7 μm) range were selected to produce conventional color images, and the three channels in the near-infrared (0.7 to 1.1 μm) range were selected to detect reflectance minima near 0.95 μm due to Fe^{2+} electronic transition absorption bands.

A multispectral (color or IR) imaging mode is effected as follows: Three spectral channels (either blue-green-red or IR1-IR2-IR3) are alternately selected with successive elevation scans while the azimuth servo is inhibited. After the third elevation scan is completed, the azimuth servo rotates the camera a small increment and the same three spectral channels are again line scanned. An azimuth sweep in this manner produces a three-channel image of the scene. A second azimuth sweep of the scene with the other three channels is required to produce a six-channel multispectral image.

The responsivity shapes of the six spectral channels depart significantly from the shapes that were hoped for. Photosensor-array size constraints and heat-sterilization

4

requirements dictated that interference-type filters be used. These filters have multiple-order transmittance peaks and are most readily made with very narrow transmittance bands (about 0.01 μm for visible wavelength filters). However, the Viking camera filters were desired to have transmittance half-widths from 0.05 to 0.1 μm and an average pass-band transmittance of over 65 percent to provide adequate sensitivity. Blocking of the multiple-order transmittance peaks over the silicon-photodiode responsivity range from 0.4 to 1.1 μm was only partially successful, and, consequently, some of the channels exhibit severe out-of-band leakage (fig. 2) and a generally undesirable responsivity shape.

The undesired signal components due to out-of-band responsivity vary appreciably between channels and may further increase for some of the near-infrared channels by the time that the landers have reached Mars. The cameras are exposed to a steady low flux of neutrons and gamma rays from the lander radioisotope-thermoelectric generators during the nearly 1-year cruise from Earth to Mars. Radiation damage by the neutrons degrades the photodiode performance, particularly in the infrared region from 0.8 to 1.1 μm where the responsivity could be reduced by an estimated 15 to 40 percent.

Figure 3 shows a simplified circuit diagram of the photosensor array (PSA) and video processing electronics (VPE). Each one of the photodiodes (except the Sun diode) has its own preamplifier to convert the small output current into a usable signal. The outputs from the preamplifiers are summed into a buffer amplifier, but only one preamplifier is turned on by the camera logic at any time. The gain of the buffer amplifier, or channel gain, is determined by the input resistances. These resistances compensate for different photodiode aperture sizes (i.e., instantaneous fields of view) and filter transmittances so that the PSA output remains approximately constant (about 1.46 V) for all channels when the camera views the average Mars radiance. (See ref. 2.)

Analytical Model

The reflectance of a diffuse surface is a function of wavelength λ and of the lighting and viewing geometry. If the blue-green-red and IR1-IR2-IR3 images are obtained at nearly the same Sun angle, the lighting and viewing geometry is fixed and the multispectral image data can be used to estimate the surface reflectance as a function of wavelength. That is, the dependence on lighting and viewing geometry can be ignored and the surface radiance $N(\lambda)$ can be expressed as

$$N(\lambda) = \frac{1}{\pi} S(\lambda)\, \tau_a(\lambda)\, \rho(\lambda) \tag{1}$$

where $S(\lambda)$ is the solar irradiance, $\tau_a(\lambda)$ is the atmospheric transmittance, and $\rho(\lambda)$ is the surface reflectance which is, for each wavelength, the ratio of reflected light to incident light.

The camera photosensor-array output voltage V_i due to a spatially uniform radiance input is (ref. 2)

$$V_i = \left(\frac{\pi}{4}\right)^2 D^2 \beta_i^2 R_{fi} G_i k_{ci} \int_0^\infty N(\lambda) \tau_c(\lambda) R_i(\lambda) \, d\lambda \tag{2}$$

where D is the lens aperture diameter, β_i is the instantaneous field of view, R_{fi} is the preamplifier feedback resistance, G_i is the channel gain, k_{ci} is a radiometric calibration constant, $\tau_c(\lambda)$ is the camera optical throughput, $R_i(\lambda)$ is the responsivity (fig. 2), and the subscript i denotes the channel-dependent parameters ($i = 1, 2, \ldots, 6$). It is convenient to combine equations (1) and (2) and express equation (2) in the simplified form

$$V_i = c_i \int_0^\infty T_i(\lambda) \rho(\lambda) \, d\lambda \qquad (i = 1, 2, \ldots, 6) \tag{3}$$

The parameter c_i is a channel-dependent system calibration constant given by

$$c_i = \frac{\pi}{16} D^2 \beta_i^2 R_{fi} G_i k_{ci} t_i \qquad (i = 1, 2, \ldots, 6) \tag{4}$$

and $T_i(\lambda)$ is a channel-dependent system transfer function given by

$$T_i(\lambda) = \frac{S(\lambda) \tau_a(\lambda) \tau_c(\lambda) R_i(\lambda)}{t_i} \qquad (i = 1, 2, \ldots, 6) \tag{5a}$$

where t_i is a scaling constant chosen so that

$$\int_0^\infty T_i(\lambda) \, d\lambda = 1 \qquad (i = 1, 2, \ldots, 6) \tag{5b}$$

Figure 4 presents a plot of typical values of $S(\lambda)$, $\tau_a(\lambda)$, and $\tau_c(\lambda)$. These plots combined with the photosensor-array responsivities plotted in figure 2 yield the six channel system transfer functions $T_i(\lambda)$ plotted in figure 5.

Calibration

It is possible to estimate the calibration constants c_1, c_2, $\ldots$, c_6 by using equation (4); however, at least one factor — the radiometric calibration constant k_{ci} — is expected to change from its prelaunch calibration value by the time that the lander reaches the Martian surface. Thus, it is preferable to determine each constant c_i by using multispectral image data of a reference test chart (RTC). An RTC is shown in figure 6; it provides 11 gray patches and 3 color patches (as well as 3 tribars to check the camera frequency response).

The reflectance at normal light incidence for all 14 RTC patches is shown in figure 7. These reference reflectances (denoted by $\rho_r(\lambda)$) have a 2-sigma accuracy of ± 8 percent. Within this accuracy the reflectance at nonnormal incidence is approximately Lambertian and is given by $\rho_r(\lambda) \cos \iota$ for most incidence angles ($20^O \leq \iota \leq 60^O$). The reflectances of the gray patches relative to each other are accurate to within ± 4 percent for any incidence angle and wavelength.

The RTC patch reflectances $\rho_r(\lambda)$ with corresponding voltages $V_1^r, V_2^r, \ldots, V_6^r$ that fall within the selected camera dynamic range satisfy equation (3); that is,

$$V_i^r = c_i (\cos \iota) \int_0^\infty T_i(\lambda) \rho_r(\lambda) \, d\lambda \qquad (i = 1, 2, \ldots, 6) \qquad (6)$$

Equation (6) provides a means of estimating each calibration constant c_i. That is, c_i is the slope of the least-squares linear fit to the data points generated by the RTC patch reflectances and plotted as $(\cos \iota) \int_0^\infty T_i(\lambda) \rho_r(\lambda) \, d\lambda$ against V_i^r. Any significant departure of the data from the least-squares line gives warning that the RTC patch reflectances may have been changed by dust adhesion or abrasion.

THE REFLECTANCE ESTIMATE AS A LINEAR COMBINATION
OF BASIS FUNCTIONS

Formulation

Equations (3) describe the relationship between the six voltages $(V_1, V_2, \ldots, V_6)$ and the unknown reflectance $\rho(\lambda)$ of a material on the Martian surface. This section is concerned with formulating a technique whereby these six voltages can be used to estimate $\rho(\lambda)$.

Let $h_1(\lambda), h_2(\lambda), \ldots, h_n(\lambda)$ be a set of n known (linearly independent) basis functions with each defined for $0 \leq \lambda < \infty$, and let $x_1, x_2, \ldots, x_n$ be a set of (constant) coefficients. The function

$$\langle \rho(\lambda) \rangle = \sum_{j=1}^n x_j h_j(\lambda) \qquad (7)$$

is an estimate of $\rho(\lambda)$ provided the coefficients are chosen to minimize the error

$$\epsilon(\lambda) = \rho(\lambda) - \langle \rho(\lambda) \rangle \qquad (8)$$

If both sides of equation (8) are multiplied by $T_i(\lambda)$ and integrated, the following set of six equations (one for each channel) are obtained

$$e_i = b_i - \sum_{j=1}^{n} a_{ij} x_j \qquad (i = 1, 2, \ldots, 6) \qquad (9)$$

where

$$a_{ij} = \int_0^\infty T_i(\lambda)\, h_j(\lambda)\, d\lambda \qquad (10a)$$

$$b_i = \frac{V_i}{c_i} = \int_0^\infty T_i(\lambda)\, \rho(\lambda)\, d\lambda \qquad (10b)$$

and

$$e_i = \int_0^\infty T_i(\lambda)\, \epsilon(\lambda)\, d\lambda \qquad (10c)$$

The error terms e_i provide a quantitative measure of the accuracy with which the estimate $\langle \rho(\lambda) \rangle$ represents the actual spectral reflectance $\rho(\lambda)$. The coefficients $x_1, x_2, \ldots, x_n$ should be chosen to minimize each term $|e_i|$.

In general, the best estimate $\langle \rho(\lambda) \rangle$ of the actual spectral reflectance $\rho(\lambda)$ is obtained if $e_i = 0$ for $i = 1, 2, \ldots, 6$. Mathematically, this means that both $\rho(\lambda)$ and $\langle \rho(\lambda) \rangle$ satisfy equations (3); and, physically, this means that two materials with reflectances $\rho(\lambda)$ and $\langle \rho(\lambda) \rangle$ generate indistinguishable camera multispectral responses. Setting $e_i = 0$ for $i = 1, 2, \ldots, 6$ in equations (9) yields the following set of six linear equations with n unknowns $x_1, x_2, \ldots, x_n$:

$$b_i = \sum_{j=1}^{n} a_{ij} x_j \qquad (i = 1, 2, \ldots, 6) \qquad (11)$$

If $n = 6$ (i.e., the number of basis functions is equal to the number of spectral channels) and if the resultant 6×6 matrix A with elements a_{ij} is nonsingular (i.e., the inverse matrix A^{-1} exists), then the set of equations (11) has a unique solution $x_1, x_2, \ldots, x_6$ and the (indistinguishable) estimate $\langle \rho(\lambda) \rangle$ is uniquely determined by equation (7). The requirement that the matrix A be nonsingular is not restrictive. It simply means that the basis functions $h_1(\lambda), h_2(\lambda), \ldots, h_6(\lambda)$ and the system transfer functions $T_1(\lambda), T_2(\lambda), \ldots, T_6(\lambda)$ must be chosen in such a fashion that each reflectance $\rho(\lambda)$ has one and only one indistinguishable estimate $\langle \rho(\lambda) \rangle$.

Basis Functions

The choice of basis functions is critical. Three appropriate choices are discussed in this section. In each case estimates $\langle \rho(\lambda) \rangle$ are constructed for eight materials that can be reasonably expected on the Martian surface as well as for the three RTC color patches and one RTC gray patch (No. 5). The true (normal) reflectance for these eight materials is presented in figure 8.

Polynomials.- If the basis functions are chosen to be $h_1(\lambda) = 1$, $h_2(\lambda) = \lambda$, . . ., $h_6(\lambda) = \lambda^5$, then the estimate

$$\langle \rho(\lambda) \rangle = \sum_{j=1}^{6} x_j \lambda^{j-1}$$

is a fifth degree polynomial in the variable λ with coefficients x_j. The corresponding elements a_{ij} of the square matrix A are given by

$$a_{ij} = \int_0^\infty T_i(\lambda) \, \lambda^{j-1} \, d\lambda$$

The matrix is nonsingular.

Figures 9 and 10 present the indistinguishable fifth degree polynomial estimates for the reflectance curves of the eight test materials and the four RTC patches, respectively. In each case the estimate is plotted for the effective range of the six channels, namely, $0.4 \leq \lambda \leq 1.1$ μm. The estimate is shown as a continuous curve and the actual reflectance as a sequence of small circles.

For computational purposes the 6 system transfer functions and 12 test reflectances were measured at 71 equally spaced wavelengths $\lambda = 0.4, 0.41, 0.42, . . ., 1.09, 1.1$. Each system transfer function was assumed to be zero outside the interval $0.4 \leq \lambda \leq 1.1$, and, consequently, all integrals were limited to this range. Simpson's rule was used throughout to evaluate the coefficients a_{ij} given by equation (10a) and the spectral samples b_i given by equation (10b).

The polynomial estimates generally agree well with the actual reflectances in a reduced domain, say $0.50 \leq \lambda \leq 1.00$. Least agreement occurs when the reflectance is most complex, that is, for the three RTC color patches. There is a pronounced tendency for the estimation error $|\epsilon(\lambda)|$ (eq. (8)) to become large as the endpoints ($\lambda = 0.4$ and $\lambda = 1.1$) are approached.

Cubic splines.- A more modern and usually better method for fitting curves to data involves the use of a cubic spline. A cubic spline is a curve defined on a sequence of subintervals; the endpoints of these subintervals are known as knots. On each subinterval

9

the curve is a cubic polynomial, and at the knots the adjacent polynomials are joined in such a fashion that the resulting curve (the cubic spline) is continuous with continuous first and second derivatives.

The knots used for all the calculations in this paper are located at the wavelengths

$$\bar{\lambda}_j = 0.45 + (j - 1)\Delta \qquad (j = 1, 2, \ldots, 6)$$

where the spacing is $\Delta = 0.12\ \mu m$. The basis functions are given by (ref. 3)

$$h_j(\lambda) = C\left(\lambda - \bar{\lambda}_j\right) \qquad (j = 1, 2, \ldots, 6)$$

where $C(\lambda)$ is the function defined by (see fig. 11(a))

$$C(\lambda) = \begin{cases} \dfrac{1}{6\Delta^3}\left[\Delta^3 + 3\Delta^2(\Delta - |\lambda|) + 3\Delta(\Delta - |\lambda|)^2 - 3(\Delta - |\lambda|)^3\right] & (|\lambda| \leqq \Delta) \\[2ex] \dfrac{1}{6\Delta^3}(2\Delta - |\lambda|)^3 & (\Delta < |\lambda| < 2\Delta) \\[2ex] 0 & (|\lambda| \geqq 2\Delta) \end{cases}$$

On each subinterval (of width Δ), $C\left(\lambda - \bar{\lambda}_j\right)$ is a cubic polynomial in λ; and at each knot, $C\left(\lambda - \bar{\lambda}_j\right)$ is continuous with continuous first and second derivatives. Consequently, the estimate $\sum\limits_{j=1}^{n} x_j\, C\left(\lambda - \bar{\lambda}_j\right)$ also has these properties and so it is a cubic spline. The six basis functions are shown in figure 11(b). The elements a_{ij} of the square matrix A are given by

$$a_{ij} = \int_0^\infty C\left(\lambda - \bar{\lambda}_j\right) T_i(\lambda)\, d\lambda \qquad (12)$$

The matrix is nonsingular.

Figures 12 and 13 present the indistinguishable cubic spline estimate for each of the eight materials and four RTC patches, respectively. The estimates agree well with the actual reflectances on a reduced domain, say $0.45 \leqq \lambda \leqq 1.05$. As with the polynomial estimates, the least agreement occurs for those reflectances which have the most complex shape. There is still a tendency (but less pronounced) for $|\epsilon(\lambda)|$ to become large as the endpoints are approached.

10

Natural cubic splines.- The cubic spline reflectance estimates can be improved by adding basis functions. Specifically, figure 11(b) reveals that, at any point in the interval $0.45 \leq \lambda \leq 0.57$ and $0.93 \leq \lambda \leq 1.05$, only three basis functions contribute to the estimate; whereas four basis functions contribute at any point in the interval $0.57 \leq \lambda \leq 0.93$. This situation can be corrected by adding two basis functions $h_0(\lambda)$ and $h_7(\lambda)$ centered at $\bar{\lambda}_0 = 0.33$ and $\bar{\lambda}_7 = 1.17$, respectively. The resulting estimate becomes

$$\langle \rho(\lambda) \rangle = \sum_{j=0}^{7} x_j \, C\left(\lambda - \bar{\lambda}_j\right) \tag{13}$$

The addition of the coefficients x_0 and x_7 modifies equation (11) to be

$$b_i = \sum_{j=0}^{7} a_{ij} r_j \qquad (i = 1, 2, \ldots, 6) \tag{14}$$

where the coefficients a_{ij} are given by equation (12). To determine the eight coefficients $x_0, x_1, \ldots, x_7$ it is necessary to add two equations to the six given by equations (14). A natural way to do this is to require that the cubic spline estimate given by equation (13) have a zero second derivative at the knots $\bar{\lambda}_1 = 0.45$ and $\bar{\lambda}_6 = 1.05$. The estimate then becomes what is known as a natural cubic spline.

It follows from figure 11 that the two additional equations are

$$x_0 \, C''(\Delta) + x_1 \, C''(0) + x_2 \, C''(-\Delta) = 0$$

and

$$x_5 \, C''(\Delta) + x_6 \, C''(0) + x_7 \, C''(-\Delta) = 0$$

which can be written, respectively, as

$$x_0 - 2x_1 + x_2 = 0 \tag{15a}$$

and

$$x_5 - 2x_6 + x_7 = 0 \tag{15b}$$

The 8×8 matrix $\underline{A}$ formed from A by adding rows corresponding to equations (15) is compiled in table II. The matrix is nonsingular.

If $\underline{x}$ and $\underline{b}$ denote the column vectors with elements x_0, x_1, . . ., x_7 and 0, b_1, . . ., b_6, 0, respectively, equations (14) and (15) can be written as

$$\underline{A}\underline{x} = \underline{b} \tag{16}$$

The indistinguishable natural cubic spline estimate corresponding to the samples b_1, b_2, . . ., b_6 is given by equation (13) where x_0, x_1, . . ., x_7 are determined by solving equation (16).

Figures 14 and 15 present the indistinguishable natural cubic spline estimate for each of the eight materials and four RTC patches, respectively. The estimates agree quite well with the actual reflectances on the entire domain $0.40 \leq \lambda \leq 1.10$. The agreement is generally better than that obtained with the fifth degree polynomial and cubic spline estimates, particularly at the endpoints. Thus, the results indicate a preference for the use of natural cubic spline reflectance estimates.

Notice specifically in figures 14 and 15 that, for the six relatively simple reflectances (i.e., pinacates 5 and 28A, Syrtis Major, augite, average Mars, and the RTC gray patch), the natural cubic spline estimates are excellent. Even for the three more complex reflectances (i.e., limonite, hypersthene, and olivine), the estimates are very good. The dominant features are reproduced; however, small period features are lost. Note particularly in figure 14 that the dominant absorption band (at $\lambda \approx 0.93$ μm) for hypersthene is quite accurately estimated. For those three materials in figure 15 with a very complex reflectance (i.e., the RTC blue, green, and red patches), the shape and location of the most dominant features are clearly identifiable. Thus, the RTC can serve not only as an aid for calibrating the cameras on Mars but also as a check on the validity of the estimation process for multispectral data received from Mars.

THE REFLECTANCE ESTIMATE AS A LINEAR COMBINATION
OF SYSTEM CHARACTERISTIC FUNCTIONS

It is possible to derive from equation (13) an alternate, mathematically equivalent, but generally preferable representation for the natural cubic spline estimate. This representation is

$$\langle \rho(\lambda) \rangle = \sum_{i=1}^{6} b_i f_i(\lambda) \tag{17}$$

where $b_i = V_i / c_i$ and $f_1(\lambda)$, $f_2(\lambda)$, . . ., $f_6(\lambda)$ are system characteristic functions. That is, $f_i(\lambda)$ is the (unique) indistinguishable natural cubic spline reflectance estimate

corresponding to the (idealized) multispectral sample with $b_i = 1$ and $b_j = 0$ for $j \neq i$. These six functions are presented in figure 16.

Images often cover spatially nonhomogeneous scenes. It is then desirable to extract reflectance estimates for various regions of the scene with a single set of system transfer functions $T_i(\lambda)$ and calibration constants c_i. The system characteristic functions are, therefore, fixed, and all that changes from one region of the scene to the next is the multispectral sample $(b_1, b_2, \ldots, b_6)$. In this situation, equation (17) is the most efficient method to calculate reflectance estimates for these various regions.

Although each system characteristic function is determined by all six transfer functions, each $f_i(\lambda)$ is dependent primarily on the corresponding system transfer function $T_i(\lambda)$. It is possible, with equation (17) and figure 16, to observe at each wavelength which channel (or channels) provides the primary contribution to the reflectance estimate.

Equation (17) also facilitates the assignment of a statistical confidence interval to the reflectance estimate $\langle \rho(\lambda) \rangle$. Specifically, suppose the transfer functions are known with accuracy but the true values of $b_1, b_2, \ldots, b_6$ are uncertain. (Each b_i must be estimated from digital data that are contaminated by electronic and quantization noise.) Then, the system characteristic functions are known with accuracy but each b_i is a random variable with mean $\bar{b}_i$ and variance σ_i^2. By assuming also that $b_1, b_2, \ldots, b_6$ are independent, the reflectance estimate is

$$\langle \rho(\lambda) \rangle = \sum_{i=1}^{6} \bar{b}_i f_i(\lambda)$$

and the variance of the estimate $\sigma_\rho^2(\lambda)$ is

$$\sigma_\rho^2(\lambda) = \sum_{i=1}^{6} \sigma_i^2 f_i^2(\lambda)$$

If all six variances are equal to a common value σ^2, then $\sigma_\rho^2(\lambda) = \sigma^2 F^2(\lambda)$ where the relative variance of the estimate is

$$F^2(\lambda) = \sum_{i=1}^{6} f_i^2(\lambda) \tag{18}$$

At each wavelength, the statistical confidence interval centered about $\langle \rho(\lambda) \rangle$ has a width proportional to the relative standard deviation of the estimate $F(\lambda)$. Figure 17 is a plot of $F(\lambda)$ against λ; the most reliable reflectance estimates occur at those wavelengths where $F(\lambda)$ is smallest.

To derive equation (17), recognize that equation (13) can be written as

$$\langle \rho(\lambda) \rangle = \underline{x}^T \, \underline{h}(\lambda)$$

where $(\ )^T$ denotes transpose and $\underline{h}(\lambda)$ is the column vector with components $C(\lambda - \bar{\lambda}_0)$, $C(\lambda - \bar{\lambda}_1), \ldots, C(\lambda - \bar{\lambda}_7)$. Since $\underline{A}$ is nonsingular, the inverse $\underline{A}^{-1}$ exists and $\underline{x}$ can be written as

$$\underline{x} = \underline{A}^{-1} \underline{b}$$

Combining these last two equations yields

$$\langle \rho(\lambda) \rangle = \underline{b}^T \left(\underline{A}^T \right)^{-1} \underline{h}(\lambda)$$

The 8×8 matrix $\left(\underline{A}^T \right)^{-1}$ transforms the natural cubic-spline basis set into a new set of basis functions $f_0(\lambda), \ f_1(\lambda), \ldots, \ f_7(\lambda)$ where $\underline{f}(\lambda)$ is a column vector with the new basis functions as its components and

$$\underline{f}(\lambda) = \left(\underline{A}^T \right)^{-1} \underline{h}(\lambda)$$

Since the first and last components of $\underline{b}$ are zero, $f_0(\lambda)$ and $f_7(\lambda)$ contribute nothing to the estimate and

$$\langle \rho(\lambda) \rangle = \underline{b}^T \, \underline{f}(\lambda) = \sum_{i=1}^{6} b_i \, f_i(\lambda)$$

which is equation (17).

THE REFLECTANCE ESTIMATE FOR A SYSTEM
WITH IMPULSE TRANSFER FUNCTIONS

The technique discussed herein produces reflectance estimates when the system transfer functions have an irregular shape with appreciable out-of-band transmittance. It is informative to observe what this technique reduces to in the idealized situation where each system transfer function can be represented as an impulse function, thereby producing a data point for each channel by associating a reflectance value with a distinct wavelength.

Suppose that

$$T_i(\lambda) = \delta\left(\lambda - \lambda_i\right) \qquad\qquad (i = 1, 2, \ldots, 6)$$

14

where the impulse system transfer functions occur at the discrete wavelengths $\lambda_1, \lambda_2, \ldots, \lambda_6$. Equations (10a), (10b), and (10c) become, respectively,

$$a_{ij} = \int_0^\infty \delta(\lambda - \lambda_i) \, h_j(\lambda) \, d\lambda = h_j(\lambda_i)$$

$$b_i = \int_0^\infty \delta(\lambda - \lambda_i) \, \rho(\lambda) \, d\lambda = \rho(\lambda_i)$$

and

$$e_i = \int_0^\infty \delta(\lambda - \lambda_i) \, \epsilon(\lambda) \, d\lambda = \epsilon(\lambda_i)$$

The elements a_{ij} and samples b_i are then the actual values of the basis functions $h_j(\lambda)$ and reflectance $\rho(\lambda)$, respectively, at the wavelengths λ_i. For an indistinguishable reflectance estimate, $e_i = \epsilon(\lambda_i) = 0$ so that the reflectance estimate interpolates the data points $\rho(\lambda_1), \rho(\lambda_2), \ldots, \rho(\lambda_6)$. That is, if, for example, the natural cubic spline basis functions were used, the reflectance estimate would be a natural cubic spline which passes through the points $\rho(\lambda_1), \rho(\lambda_2), \ldots, \rho(\lambda_6)$.

Figures 18 and 19 present the reflectance estimates and figures 20 and 21 present the system characteristic functions and relative standard deviation of the estimate, respectively, for an idealized system with impulse system transfer functions located at the six interior knots of the natural cubic spline, that is, 0.45, 0.57, 0.69, 0.81, 0.93, and 1.05. If a six-channel system with impulse system transfer functions were designed to reproduce estimates best for a family of reflectances at all wavelengths $0.4 \leq \lambda \leq 1.1$ μm, the impulses should probably be evenly spaced and located at or near these six wavelengths.

Comparison of figures 14 and 15 with 18 and 19 reveals that both sets of estimates are very similar and that neither is consistently superior. This observation is supported by the data in table III which presents the root-mean-square (rms) error between the actual reflectance $\rho(\lambda)$ and the estimated reflectance $\langle \rho(\lambda) \rangle$ corresponding to figures 14, 15, 18, and 19. Three important conclusions can be made:

(1) The proposed technique for constructing reflectance estimates completely compensates for system transfer functions with an irregular shape and appreciable out-of-band transmittance.

(2) The loss of small period features in the reflectance estimate is due to the under-sampling inherent in the limited number of spectral channels and is not due to the irregular shape and appreciable out-of-band transmittance of the system transfer functions.

(3) System transfer functions with an irregular shape and appreciable out-of-band transmittance are not necessarily undesirable provided that they are properly accounted for by the reflectance estimation process.

CONCLUDING REMARKS

A technique was formulated for constructing spectral reflectance curve estimates from multispectral data obtained with the Viking lander camera. The multispectral data are limited to six spectral channels and most of these channels exhibit appreciable out-of-band response. The output of each channel was expressed as an integral function of the spectral reflectance producing six equations which were used to determine the coefficients in a representation of the spectral reflectance as a linear combination of known basis functions. Several sets of basis functions were investigated. Of these the natural cubic spline basis functions generally produced the best reflectance estimates for a variety of materials that can be reasonably expected to occur on the Martian surface.

It was found that the dominant reflectance features of these materials can be faithfully reproduced; only small period features are lost due to the undersampling inherent in the limited number of spectral channels. The technique completely compensates for system transfer functions with irregular shapes and appreciable out-of-band transmittance. Moreover, the technique may be a valuable aid in selecting the number of spectral channels and their responsivity shapes when designing a multispectral imaging system. This design approach should prove of value especially if spectral reflectance properties of interest are known a priori and if the transfer function shapes are desired to be broad to obtain good signal-to-noise ratios.

The reference test charts located on the lander consist of simple gray and complex color spectral reflectances. It was shown that the shape and location of the dominant features for the complex color reflectances are closely identifiable. Thus, the reference test chart can serve not only as a means for calibrating the cameras on Mars but also as a means for checking the validity of the estimation process for multispectral data received from Mars.

Langley Research Center
National Aeronautics and Space Administration
Hampton, VA 23665
September 13, 1976

REFERENCES

1. Huck, F. O.; McCall, H. F.; Patterson, W. R.; and Taylor, G. R.: The Viking Mars Lander Camera. Space Sci. Instrum., vol. 1, no. 2, May 1975, pp. 189-241.

2. Huck, Friedrich O.; Burcher, Ernest E.; Jobson, Daniel J.; and Wall, Stephen D.: Prediction of Viking Lander Camera Image Quality. NASA TN D-8148, 1976.

3. Prenter, P. M.: Splines and Variational Methods. John Wiley & Sons, Inc., c.1975, p. 79.

TABLE I.- GENERAL DESIGN AND PERFORMANCE CHARACTERISTICS

Characteristic	Survey	Color and IR	High resolution
Instantaneous field of view, deg	0.12	0.12	0.04
Picture-element registration error, deg . . .	±0.036	±0.013	±0.006
Absolute angle error:			
Elevation, deg	±0.3	±0.2	±0.2
Azimuth, deg	±0.15	±0.1	±0.1
Frame width:			
Elevation, deg	61.44	61.44	20.48
Azimuth (min.; max.), deg	2.5; 342.5	2.5; 342.5	2.5; 342.5
Field of view:			
Elevation, deg	100; from 40° above to 60° below horizon in 10° steps		
Azimuth, deg	342.5; in multiples of 2.5° steps		
Geometric depth of field, m	1.7 to ∞	1.7 to ∞	1.7 to ∞
In-focus distance, m	3.7	3.7	1.9, 2.7, 4.5, and 13.3
Picture elements per line	512	512	512
Bits per picture element	6	6	6
Bits per degree azimuth.	2.84×10^4	8.53×10^4	8.53×10^4
Time per degree azimuth:			
Rapid scan, s	1.84	5.52	5.52
Slow scan, min	2.0	6.0	6.0

18

TABLE II.- THE $\underline{A}$ MATRIX

$$
\begin{bmatrix}
1 & -2 & 1 & 0 & 0 & 0 & 0 & 0 \\
0.1216 & 0.5418 & 0.2539 & 0.0536 & 0.0099 & 0.0042 & 0.0106 & 0.0036 \\
0.0087 & 0.2934 & 0.5770 & 0.1035 & 0.0045 & 0.0038 & 0.0070 & 0.0020 \\
0.0024 & 0.0175 & 0.2866 & 0.5488 & 0.1386 & 0.0054 & 0.0006 & 0.0001 \\
0.0017 & 0.0056 & 0.0068 & 0.0466 & 0.4352 & 0.4490 & 0.0535 & 0.0016 \\
0.0055 & 0.0556 & 0.0663 & 0.0227 & 0.1206 & 0.5062 & 0.2172 & 0.0060 \\
0.0103 & 0.0641 & 0.0896 & 0.1262 & 0.0925 & 0.2918 & 0.2926 & 0.0327 \\
0 & 0 & 0 & 0 & 0 & 1 & -2 & 1
\end{bmatrix}
$$

TABLE III.- THE ROOT-MEAN-SQUARE DEVIATION BETWEEN

THE ACTUAL REFLECTANCE AND ITS ESTIMATE

Reflectance of —	System transfer functions	
	Actual (a)	Impulse (b)
Average Mars	0.0020	0.0023
Syrtis Major	0.0055	0.0045
Pinacates 5	0.0037	0.0045
Pinacates 28A	0.0050	0.0063
Augite	0.0024	0.0027
Limonite	0.0145	0.0186
Olivine	0.0088	0.0124
Hypersthene	0.0060	0.0050
RTC gray	0.0030	0.0027
RTC blue	0.1092	0.0990
RTC green	0.0665	0.0590
RTC red	0.0519	0.0484

[a]See figures 14 and 15.
[b]See figures 18 and 19.

UPPER
ELEVATION
ASSEMBLY

THERMAL
CONTROL BOARD
ASSEMBLY

WAVEGUIDE

OUTER HOUSING
WINDOW AND DOOR ASSEMBLY

MIRROR
ELEVATION ASSEMBLY
LENS CELL

PHOTOSENSOR ARRAY (PSA)

DUPLEX BEARINGS
TORQUE MOTOR
AZIMUTH ASSEMBLY
RESOLVER
AZIMUTH TACHOMETER
RADIAL BEARINGS
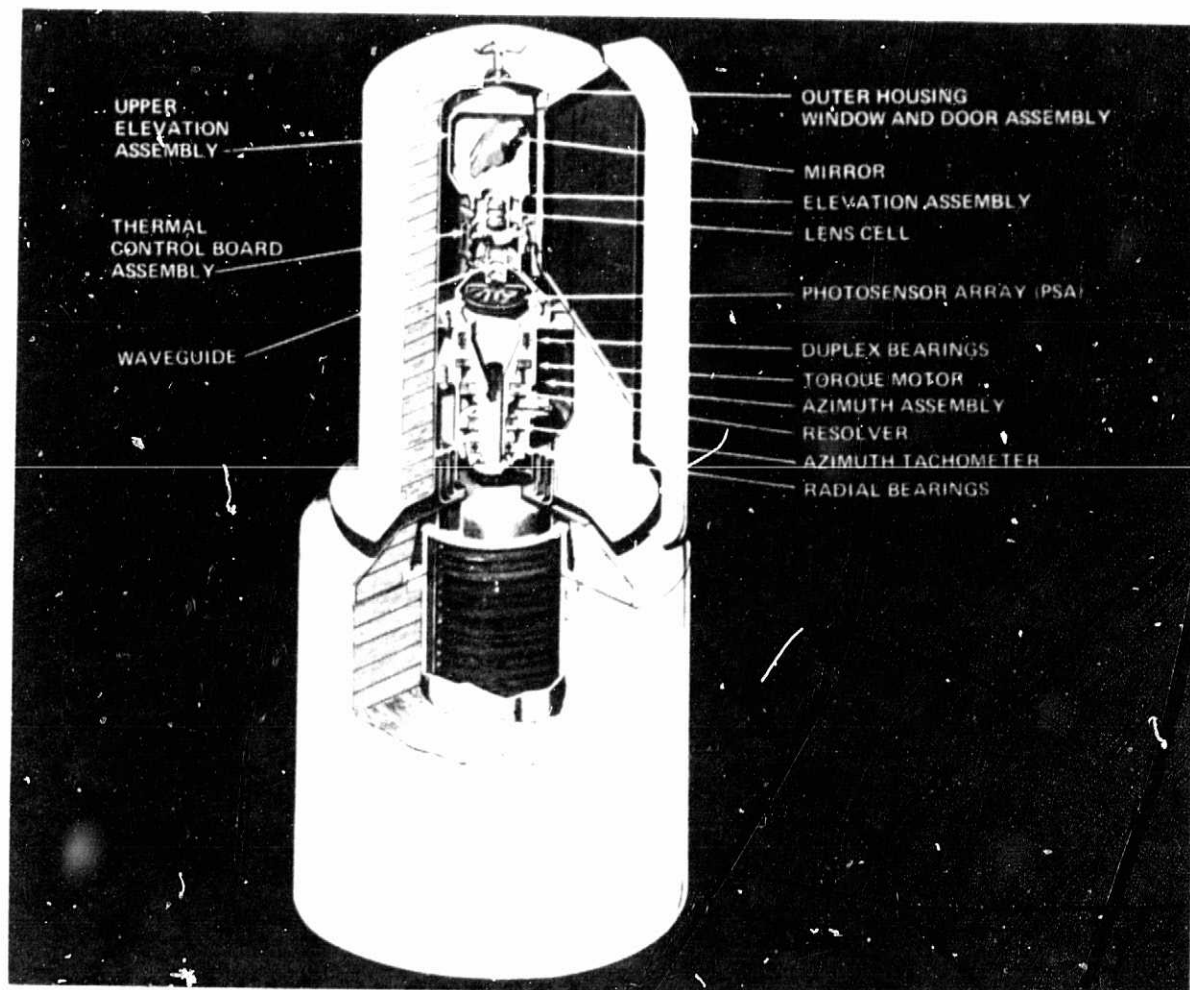
L-76-256

Figure 1.- Simplified cutaway view of the Viking lander camera.
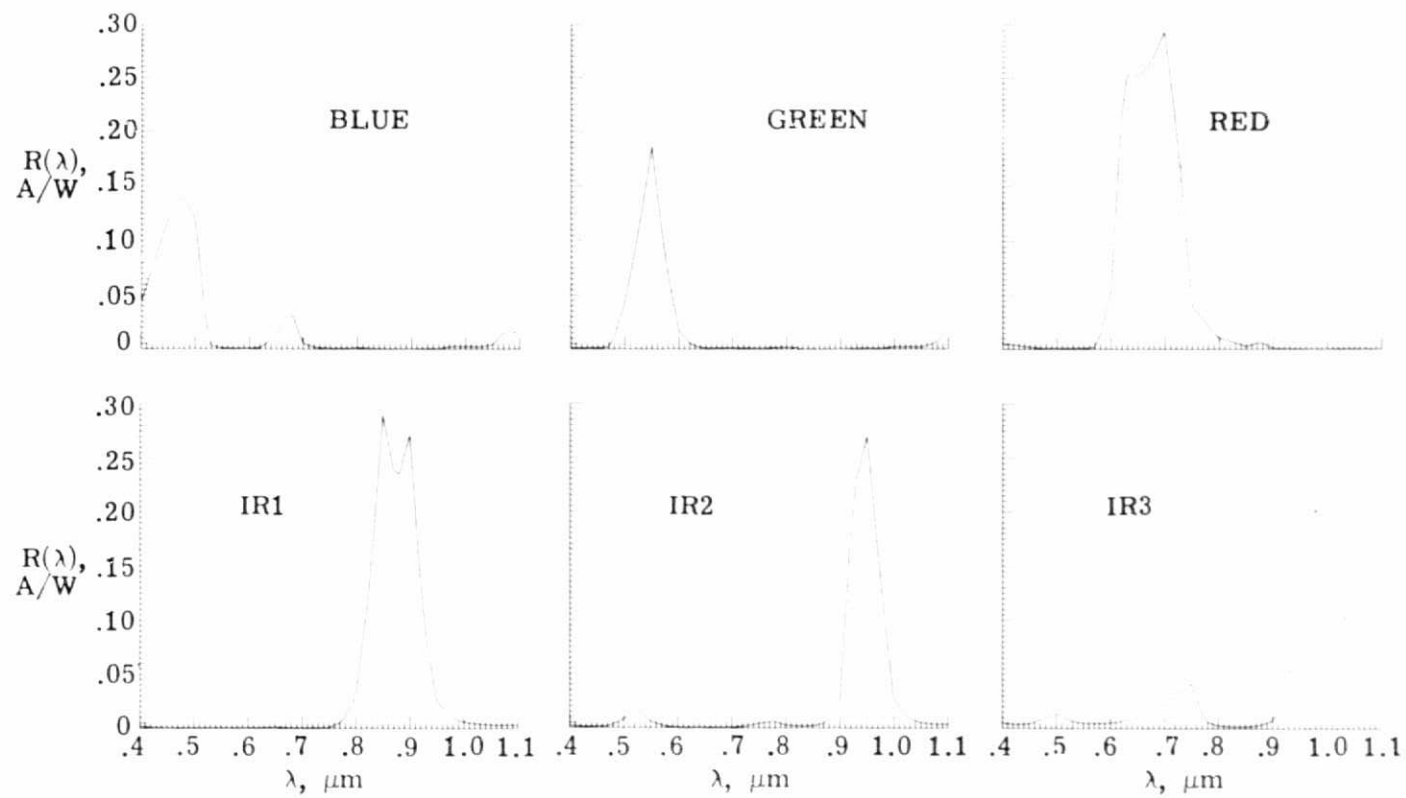
Figure 2.- Typical responsivities for the six narrowband Viking lander camera channels.
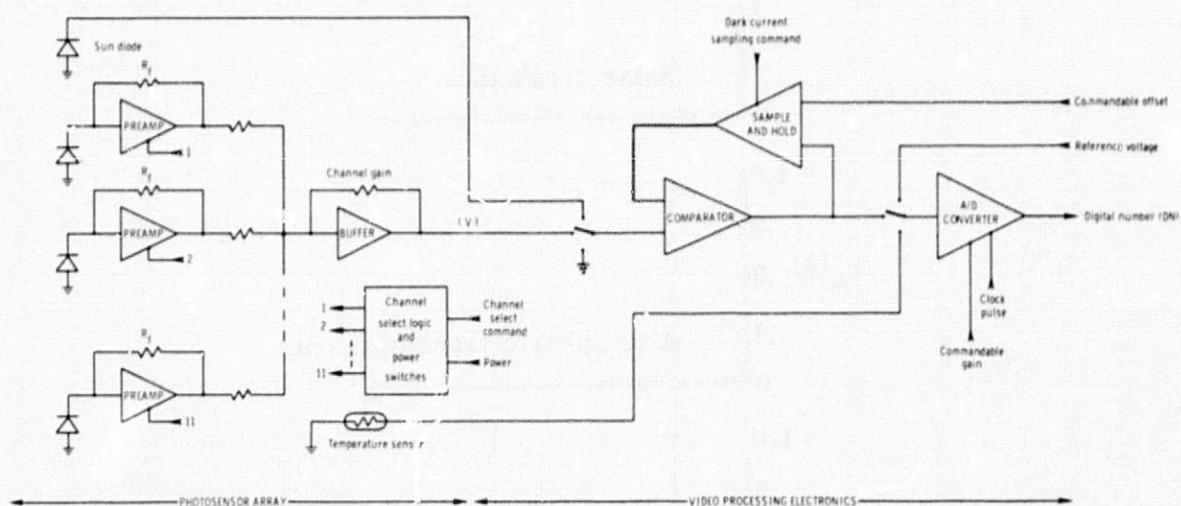
Figure 3.- Simplified circuit diagram of photosensor array (PSA)
and video processing electronics (VPE).

23
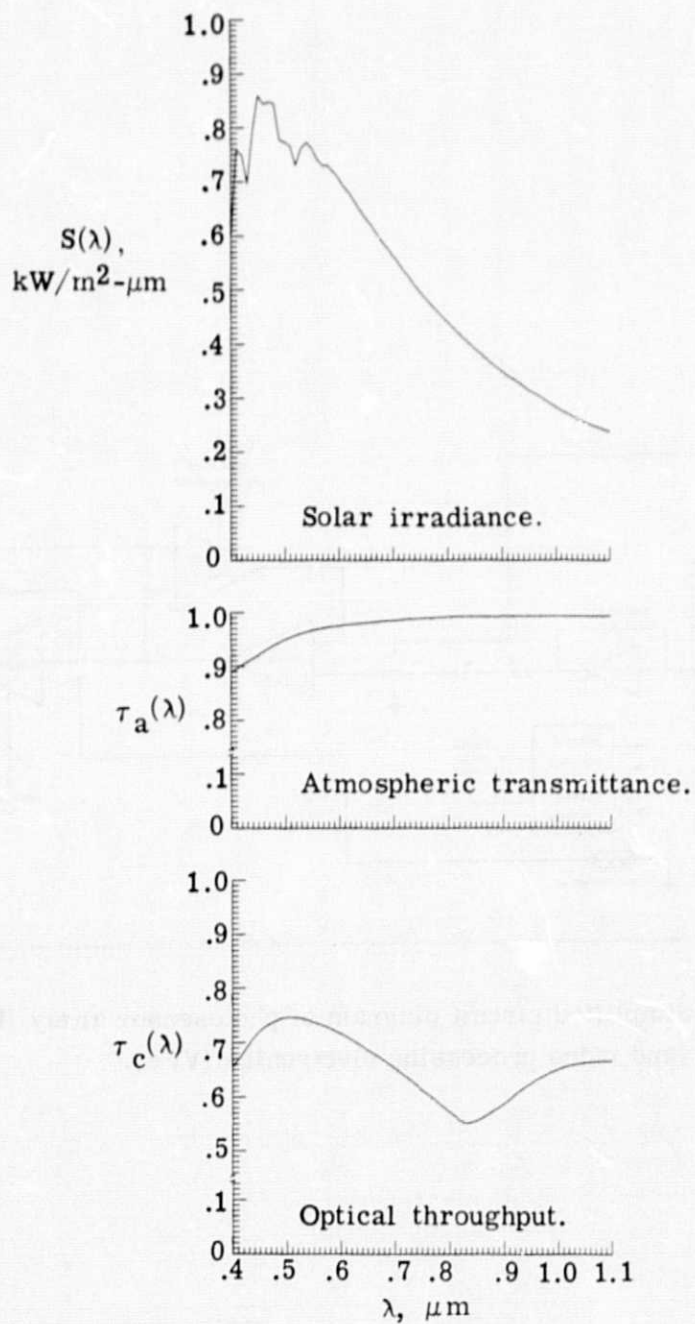
Figure 4.- Plots of $S(\lambda)$, $\tau_a(\lambda)$, and $\tau_c(\lambda)$ against λ.
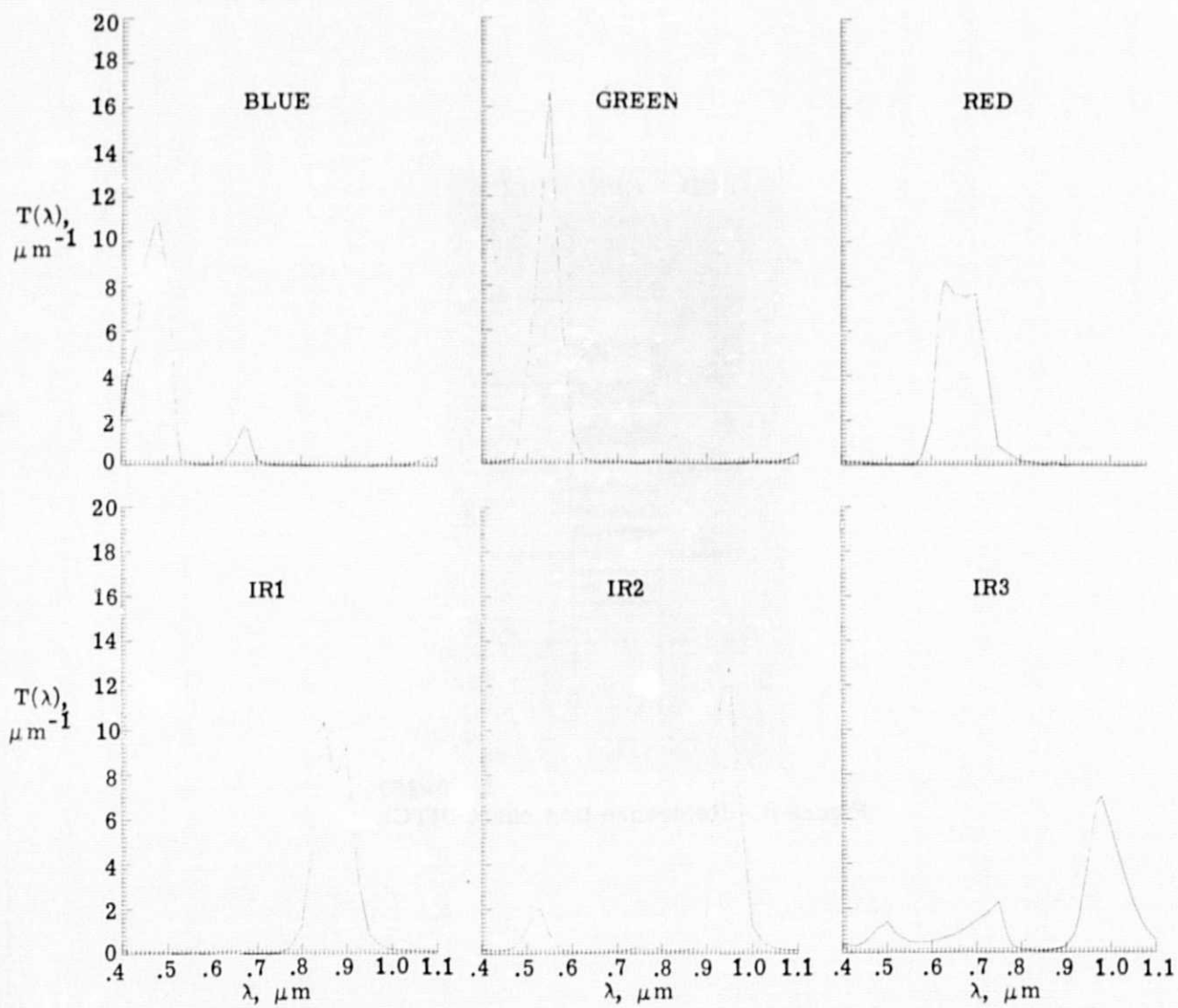
Figure 5.- Typical system transfer functions.

L-76-257
Figure 6.- Reference test chart (RTC).

26
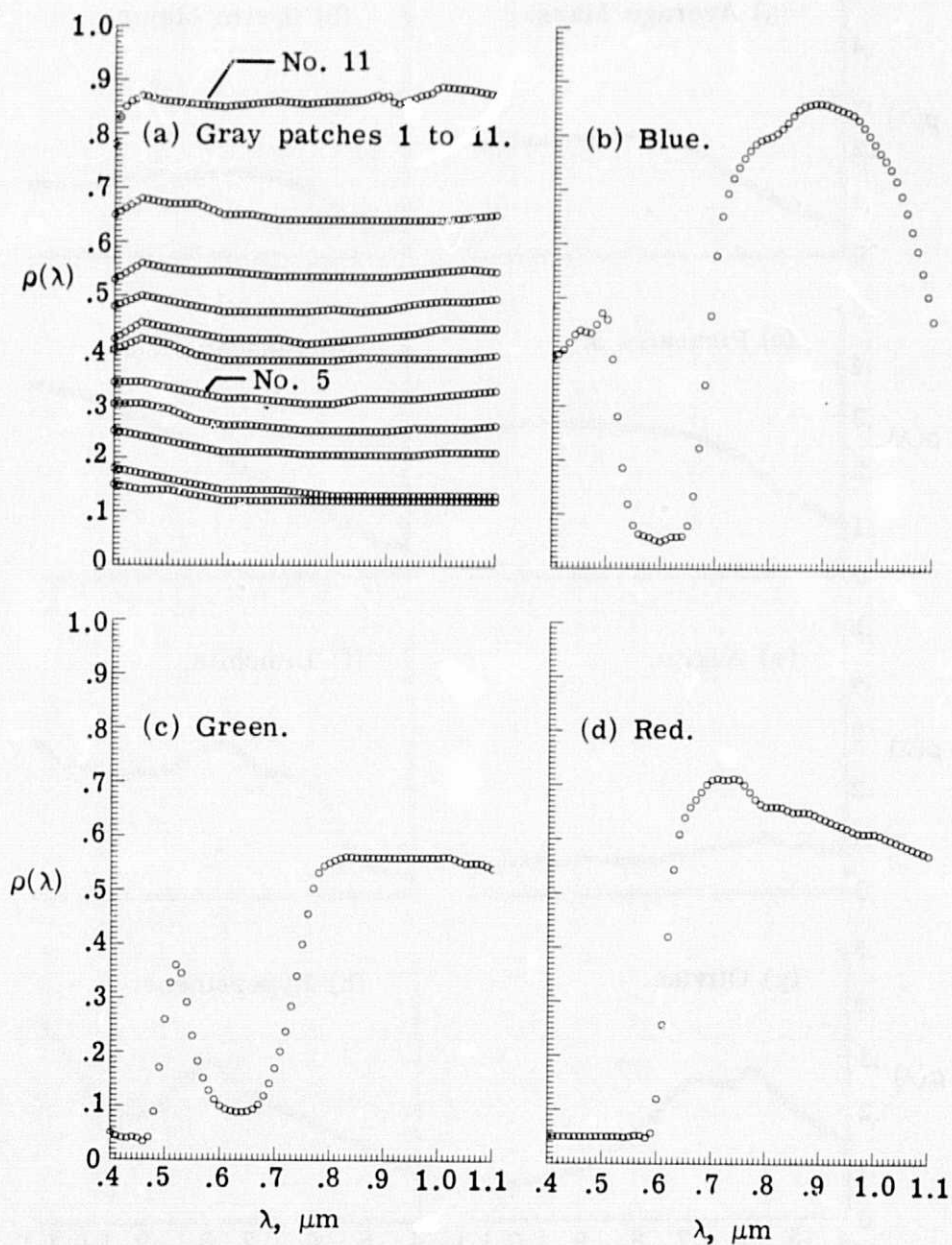
Figure 7.- Reflectances of the 11 gray and 3 color RTC patches.
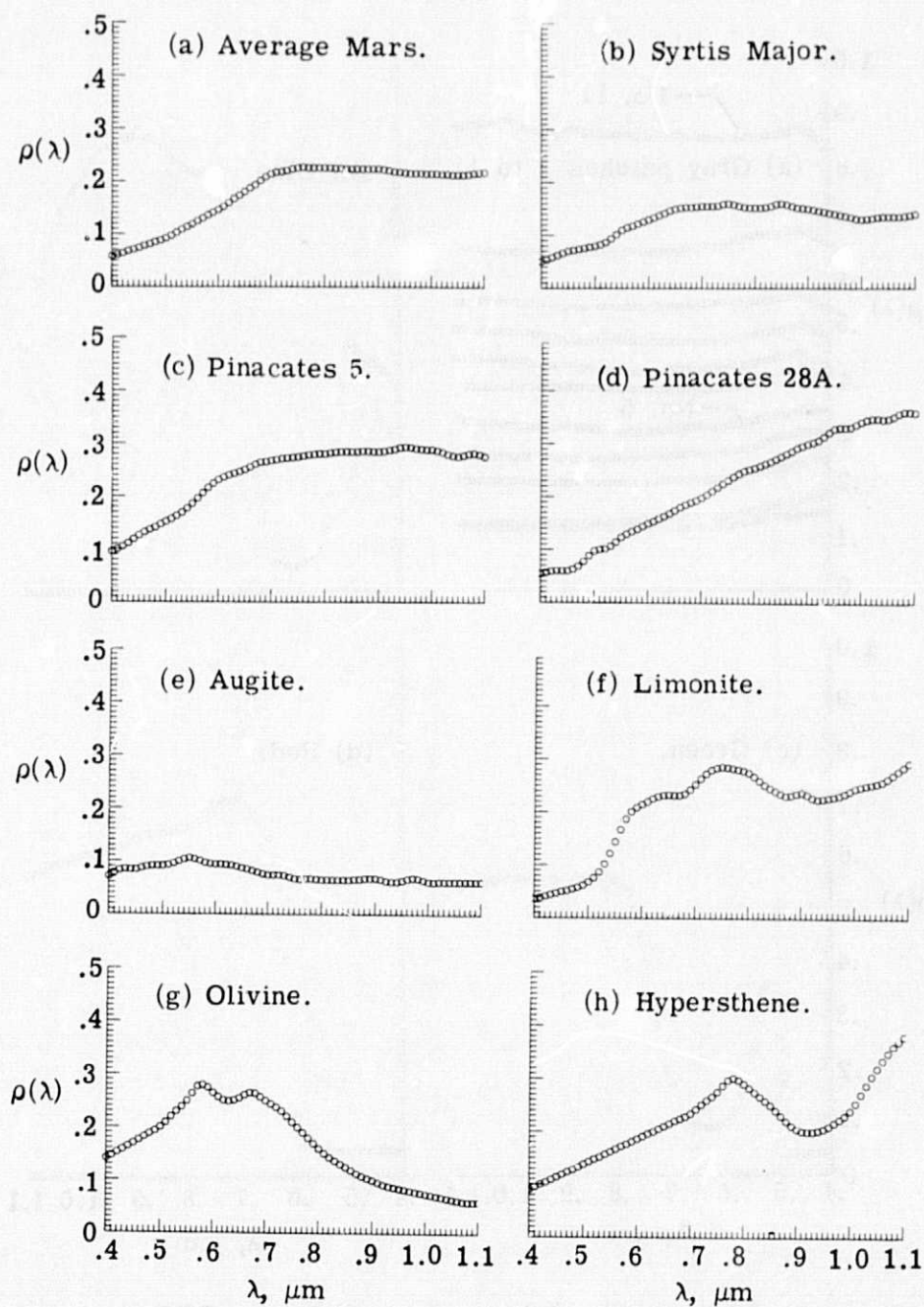
Figure 8.- Reflectances of the eight test materials.
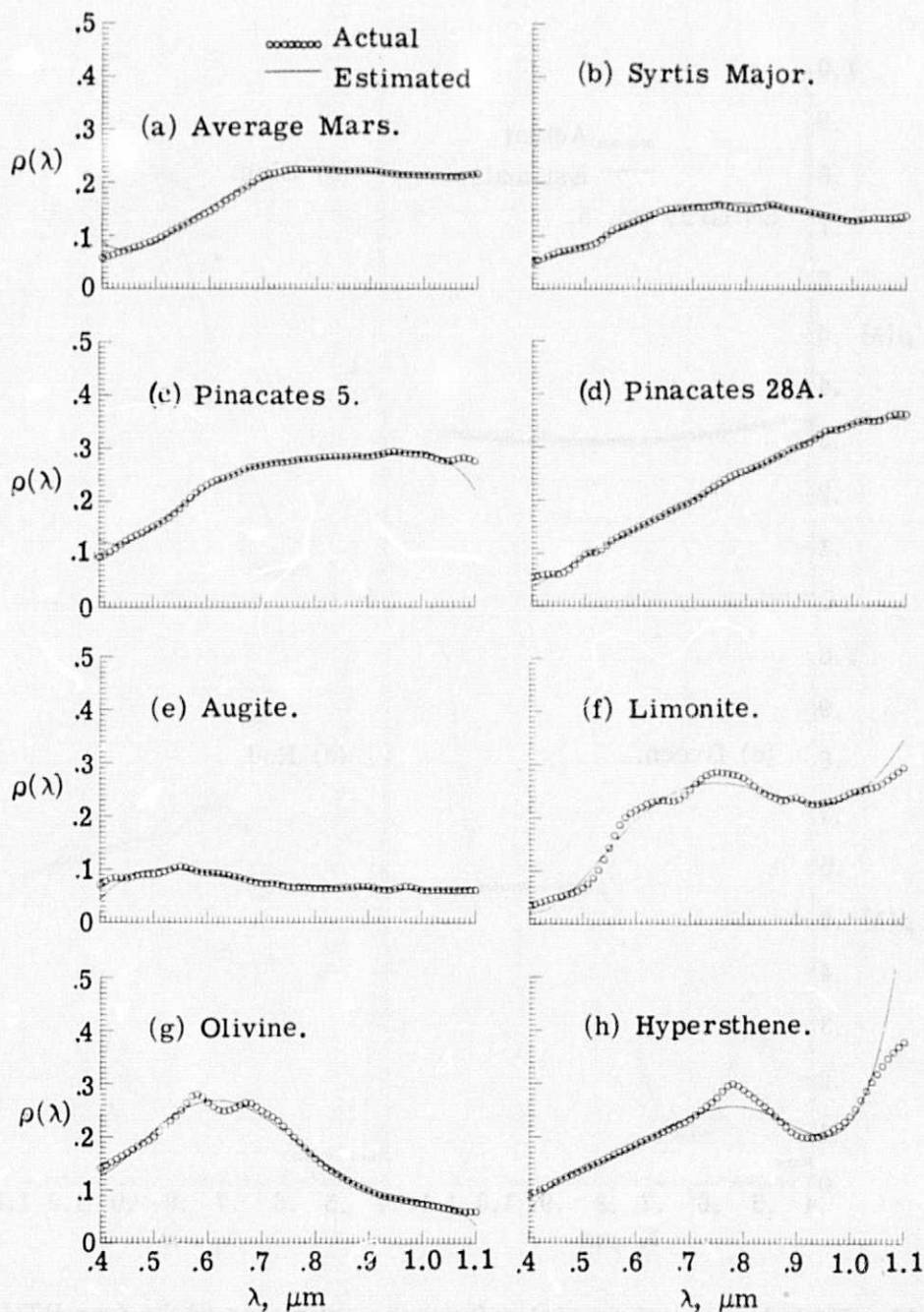
Figure 9.- Fifth degree polynomial reflectance estimates of the eight test materials.
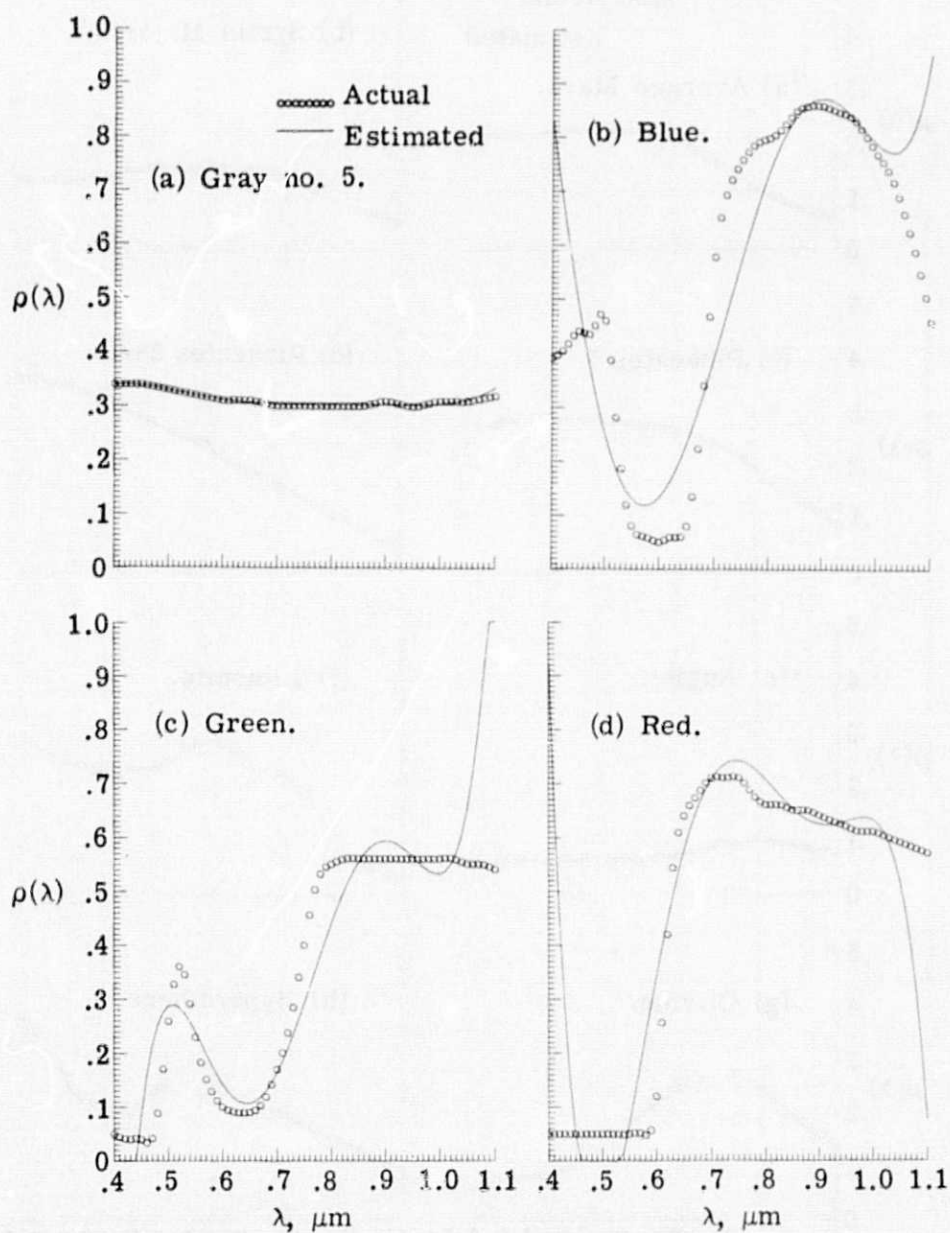
Figure 10.- Fifth degree polynomial reflectance estimates of the four RTC patches.
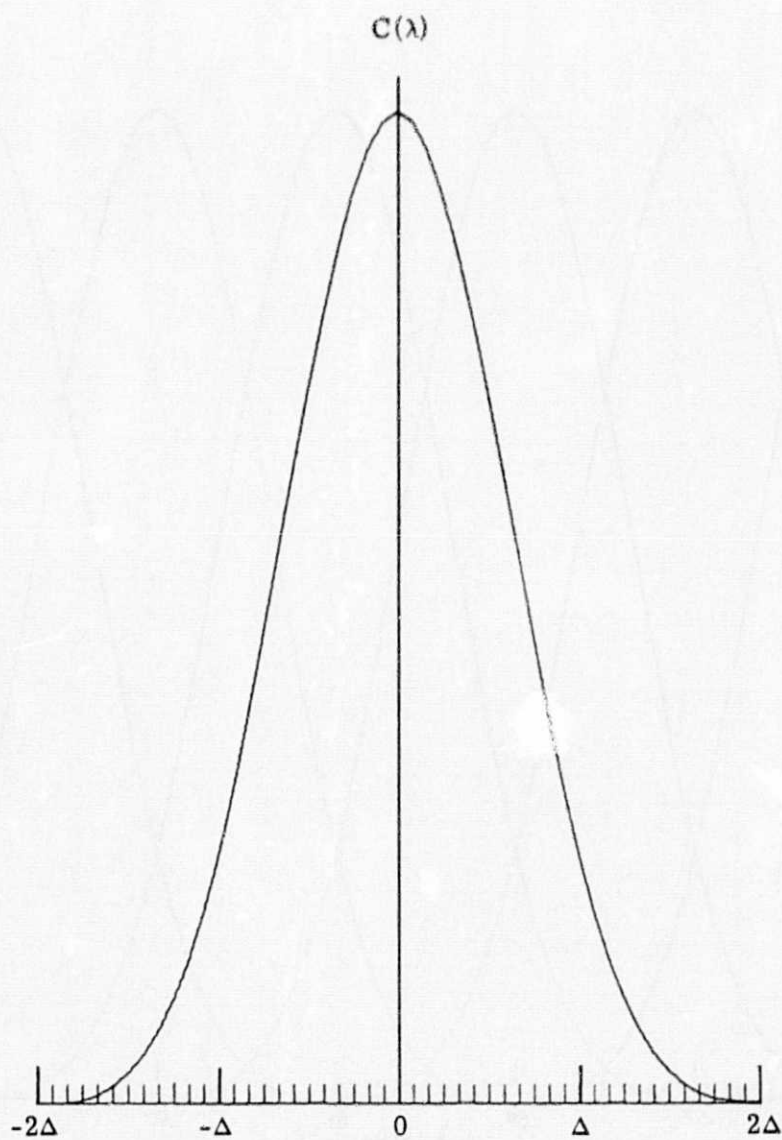
(a) The basis function $C(\lambda)$.

Figure 11.- Cubic spline basis functions.
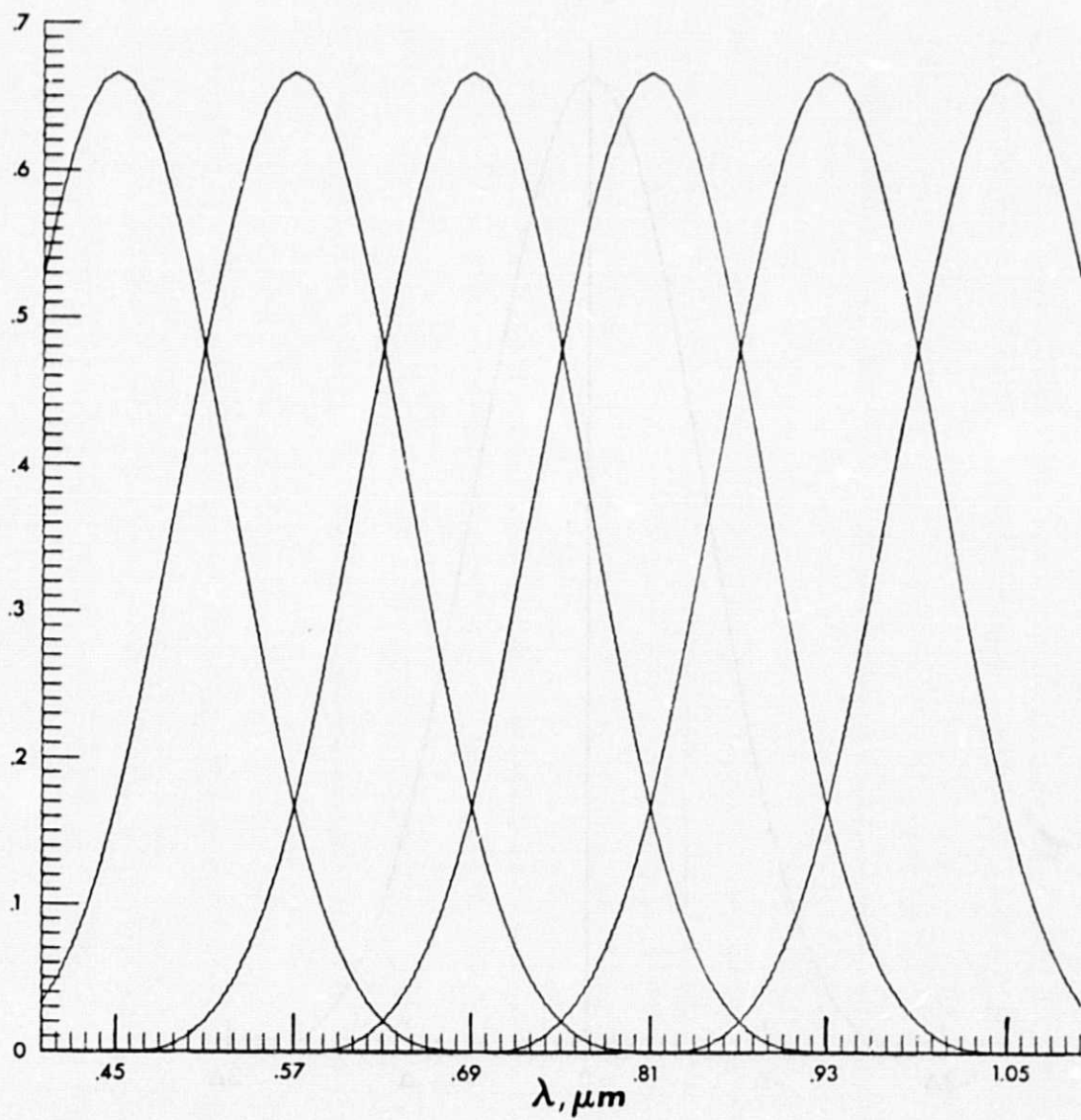
(b) Six cubic spline basis functions centered at knots 0.45, 0.57, . . ., 1.05.

Figure 11.- Concluded.
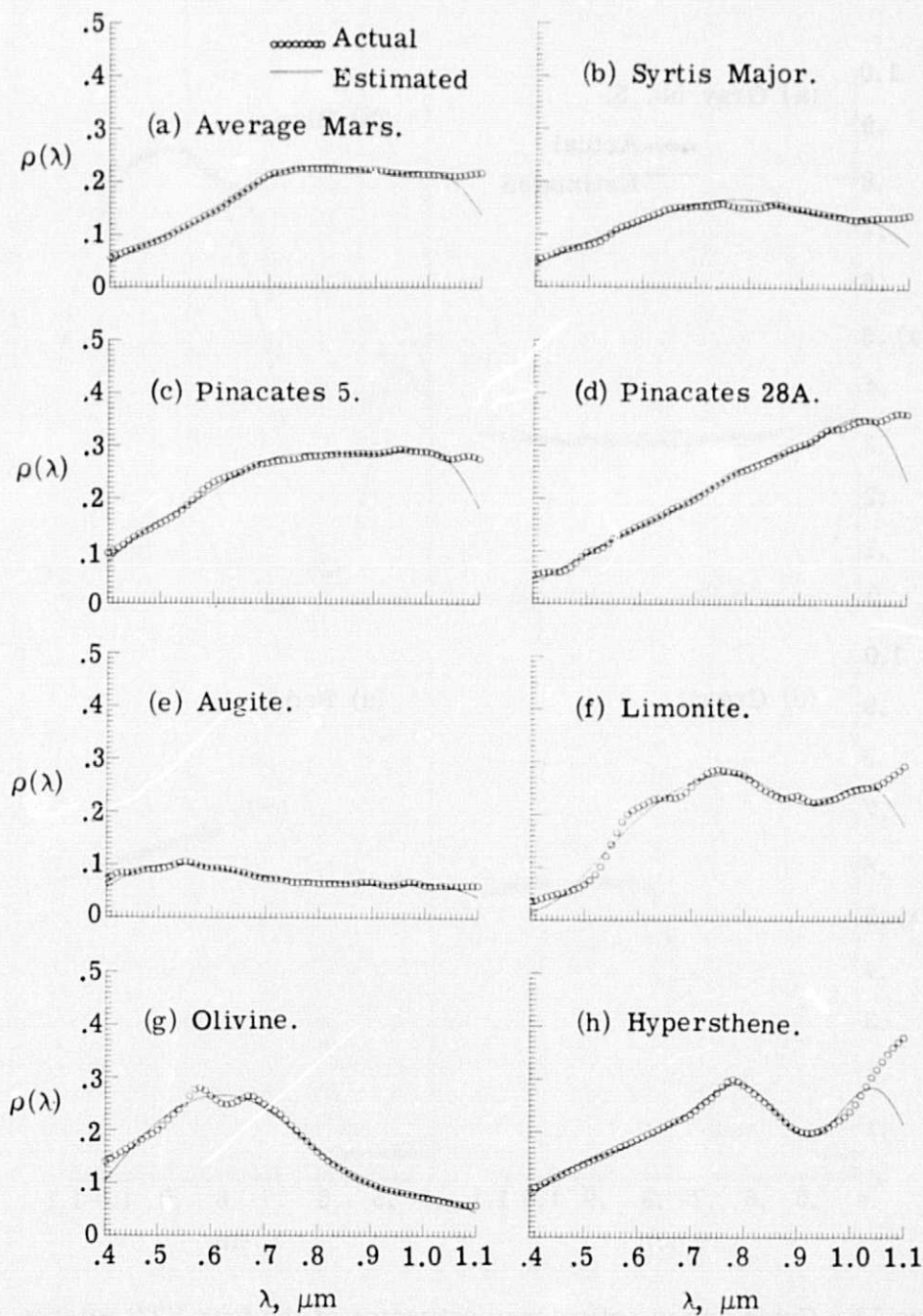
Figure 12.- Cubic spline reflectance estimates of the eight test materials.
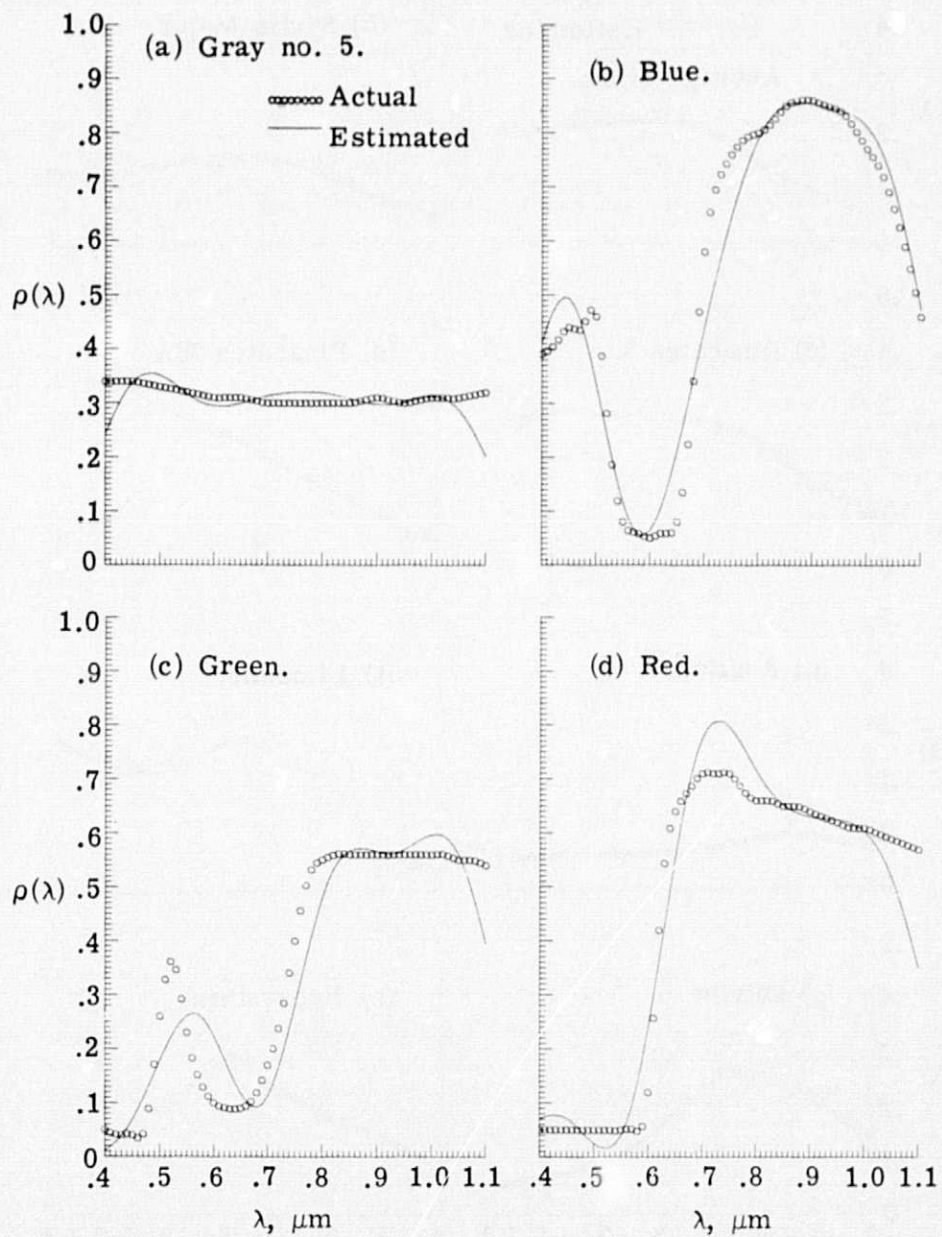
Figure 13.- Cubic spline reflectance estimates of the four RTC patches.
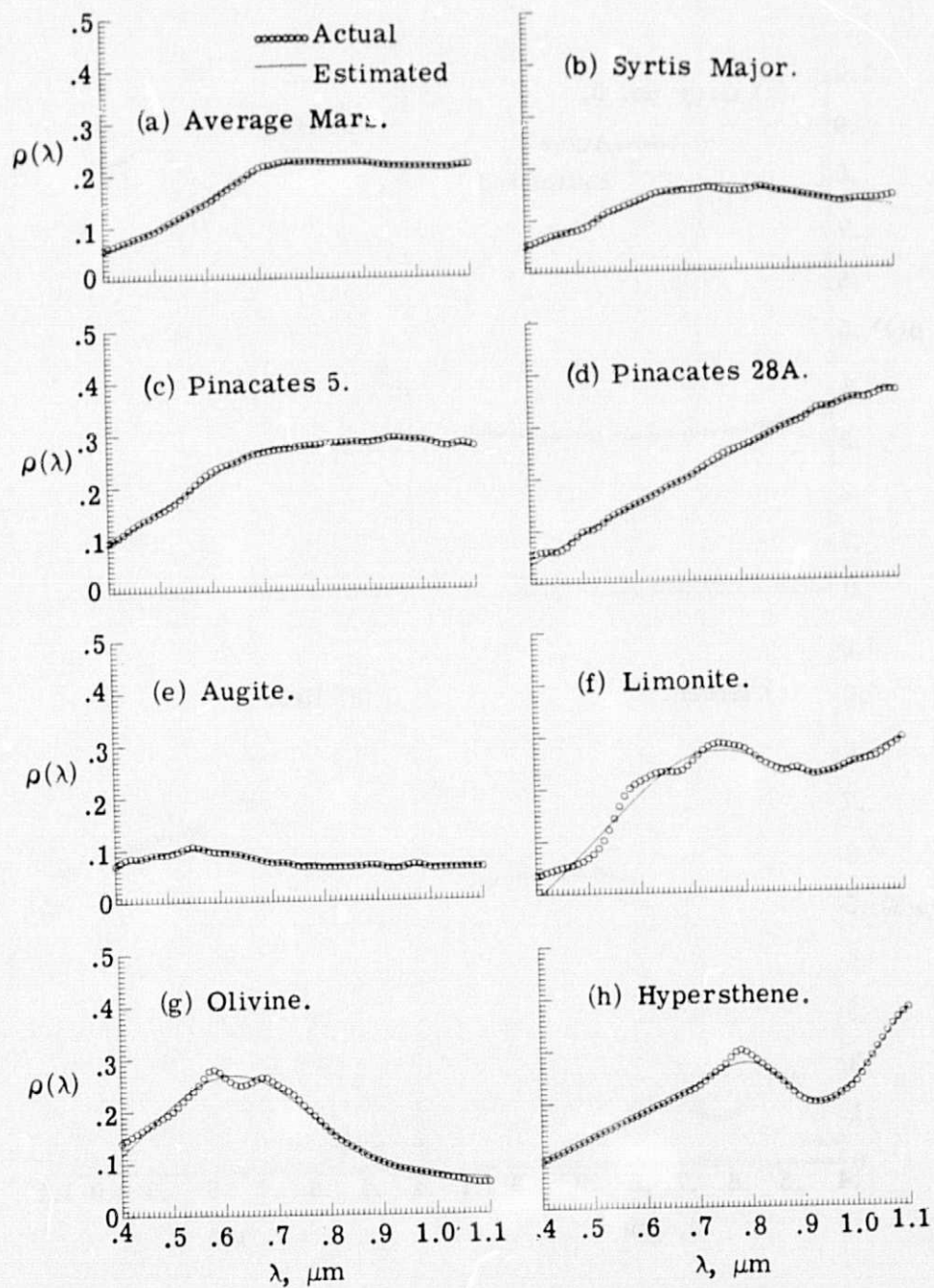
Figure 14.- Natural cubic spline reflectance estimates of the eight test materials.
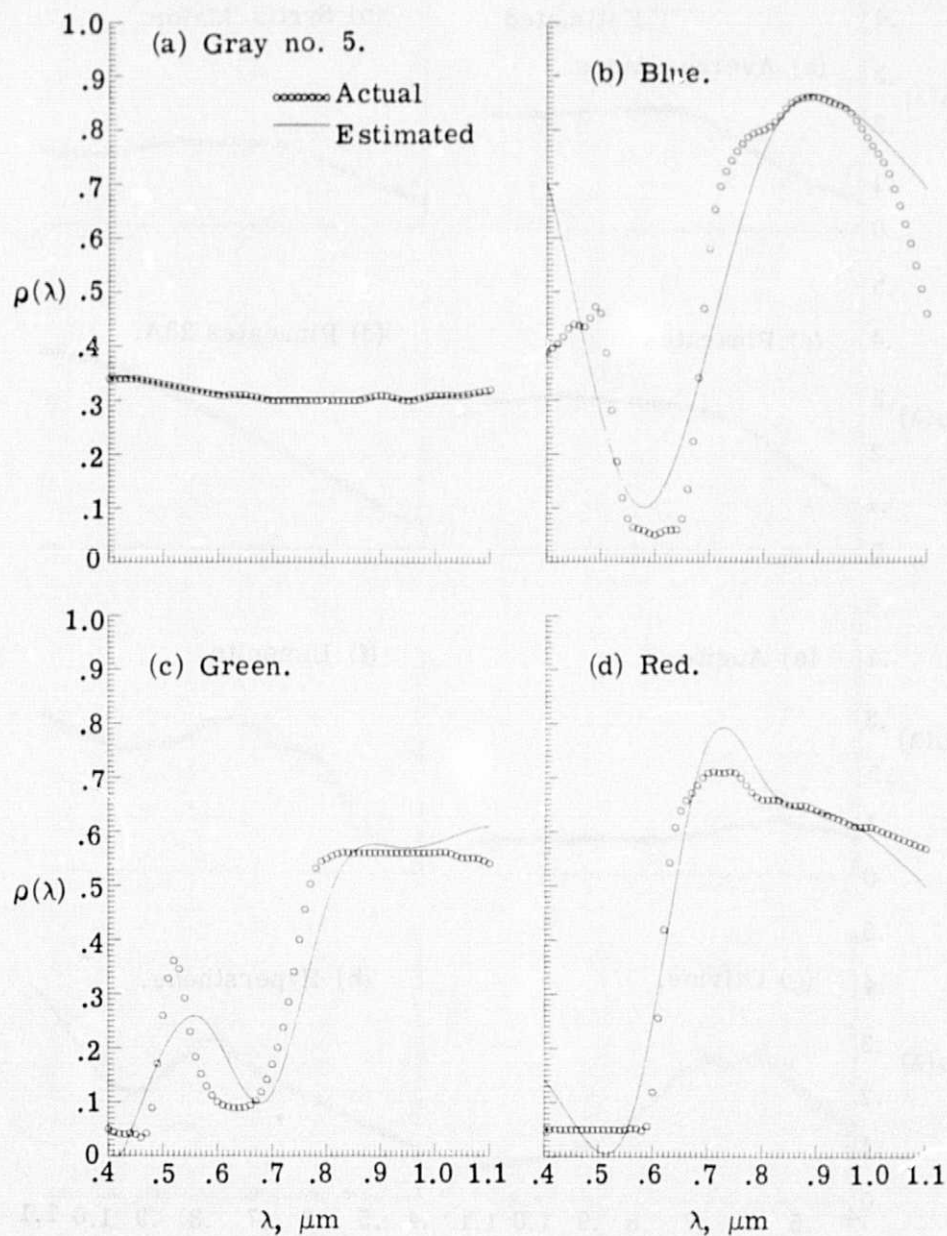
Figure 15.- Natural cubic spline reflectance estimates of the four RTC patches.
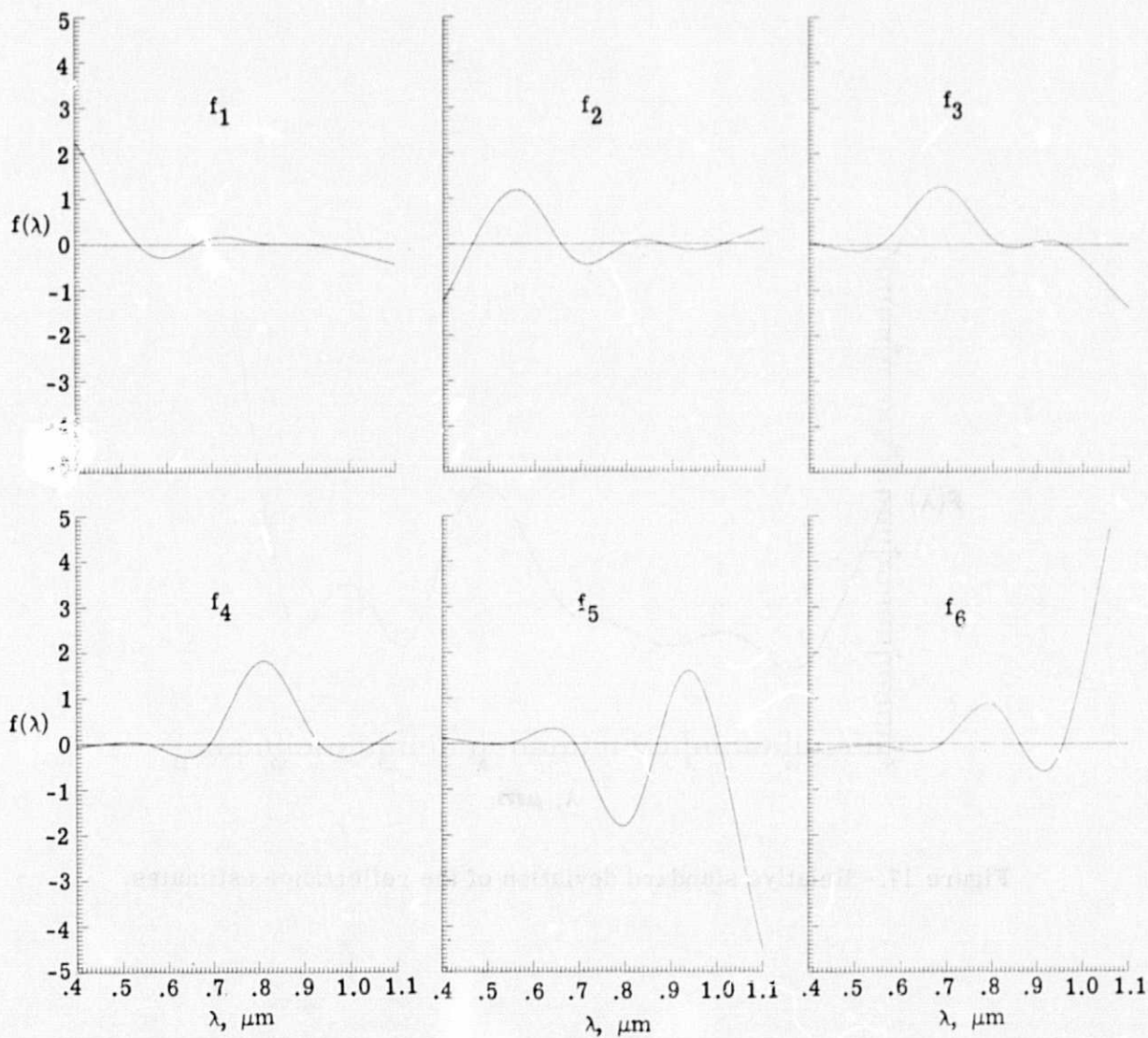
Figure 16.- System characteristic functions $f_i(\lambda)$.
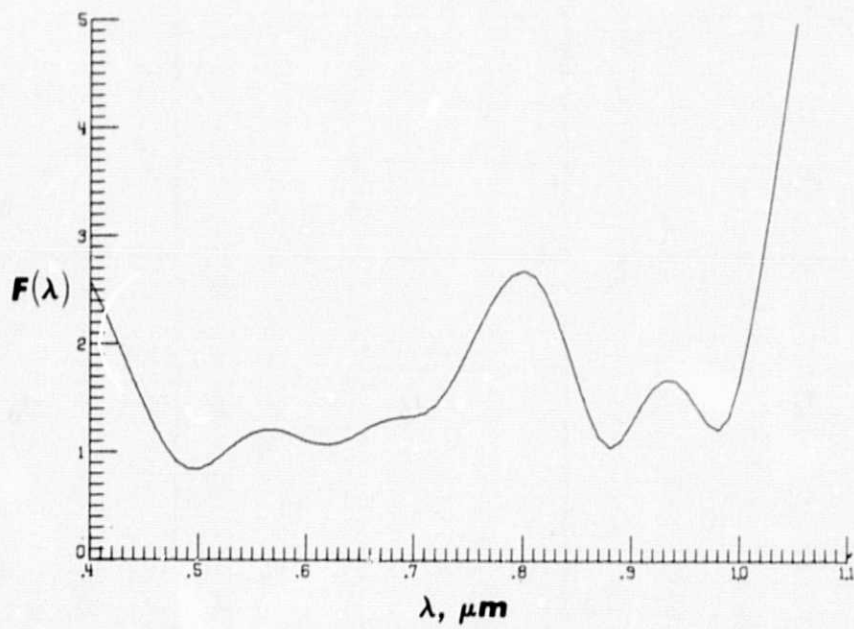
Figure 17.- Relative standard deviation of the reflectance estimates.
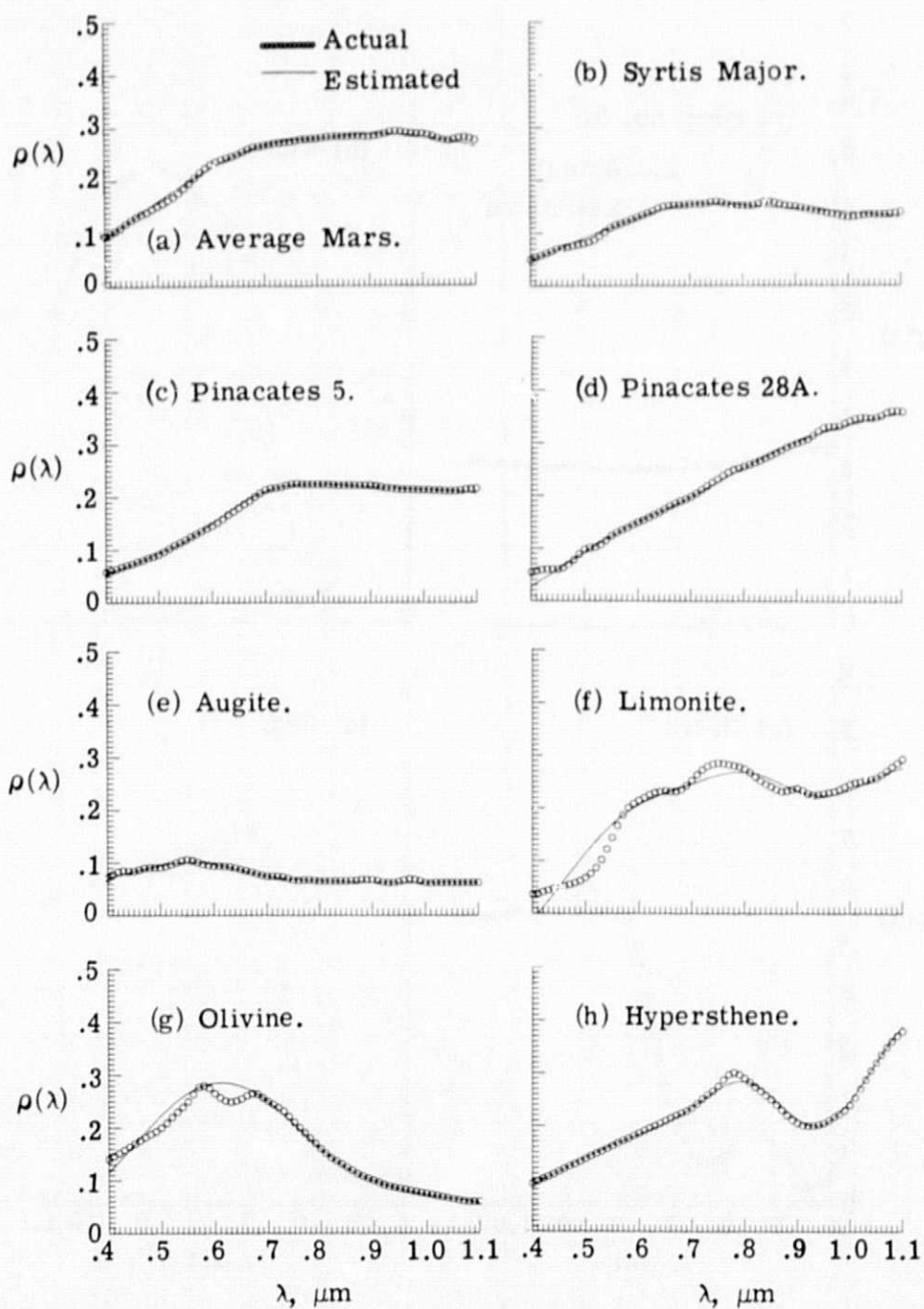
Figure 18.- Natural cubic spline reflectance estimates of the eight test materials for an idealized system with impulse system transfer functions.
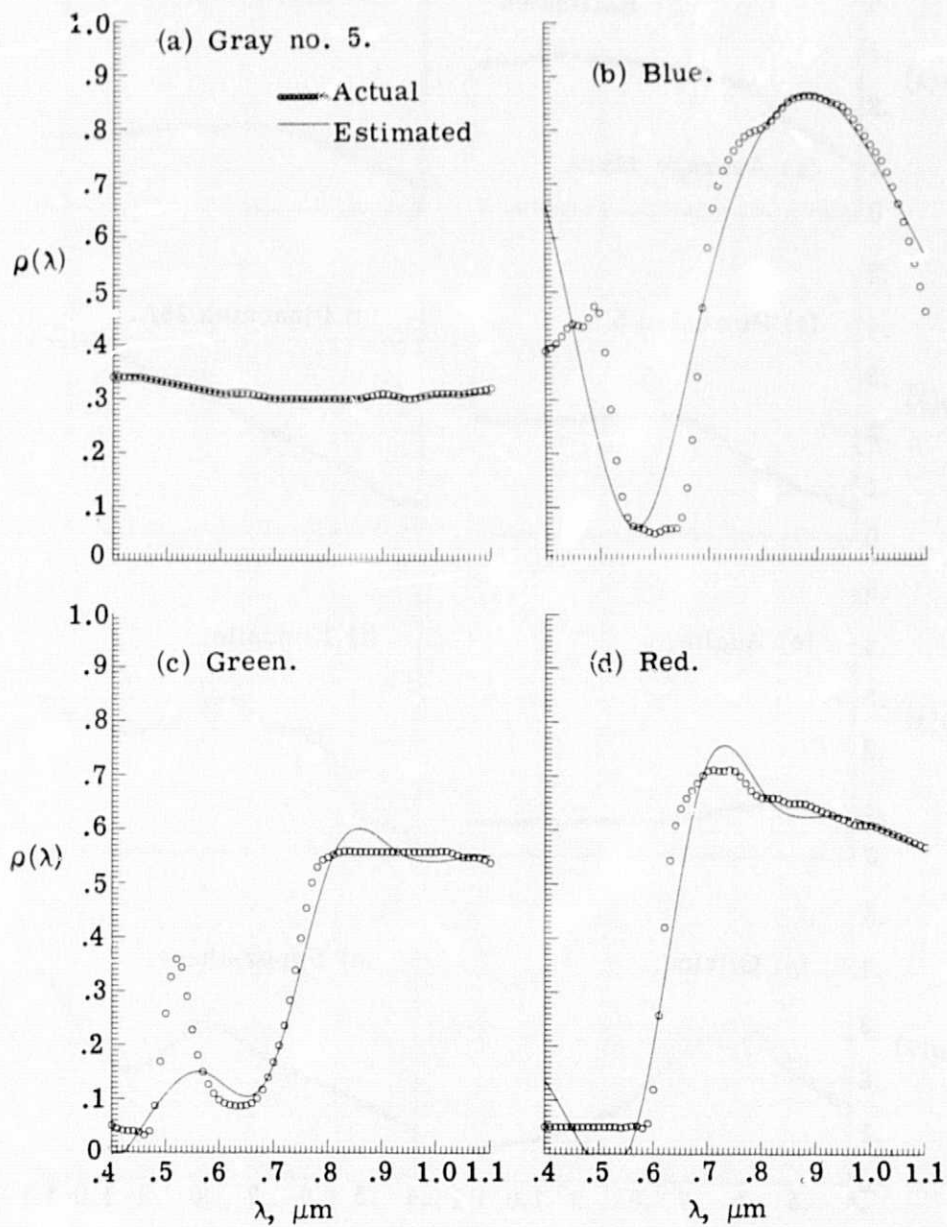
Figure 19.- Natural cubic spline reflectance estimates of the four RTC patches for an idealized system with impulse system transfer functions.
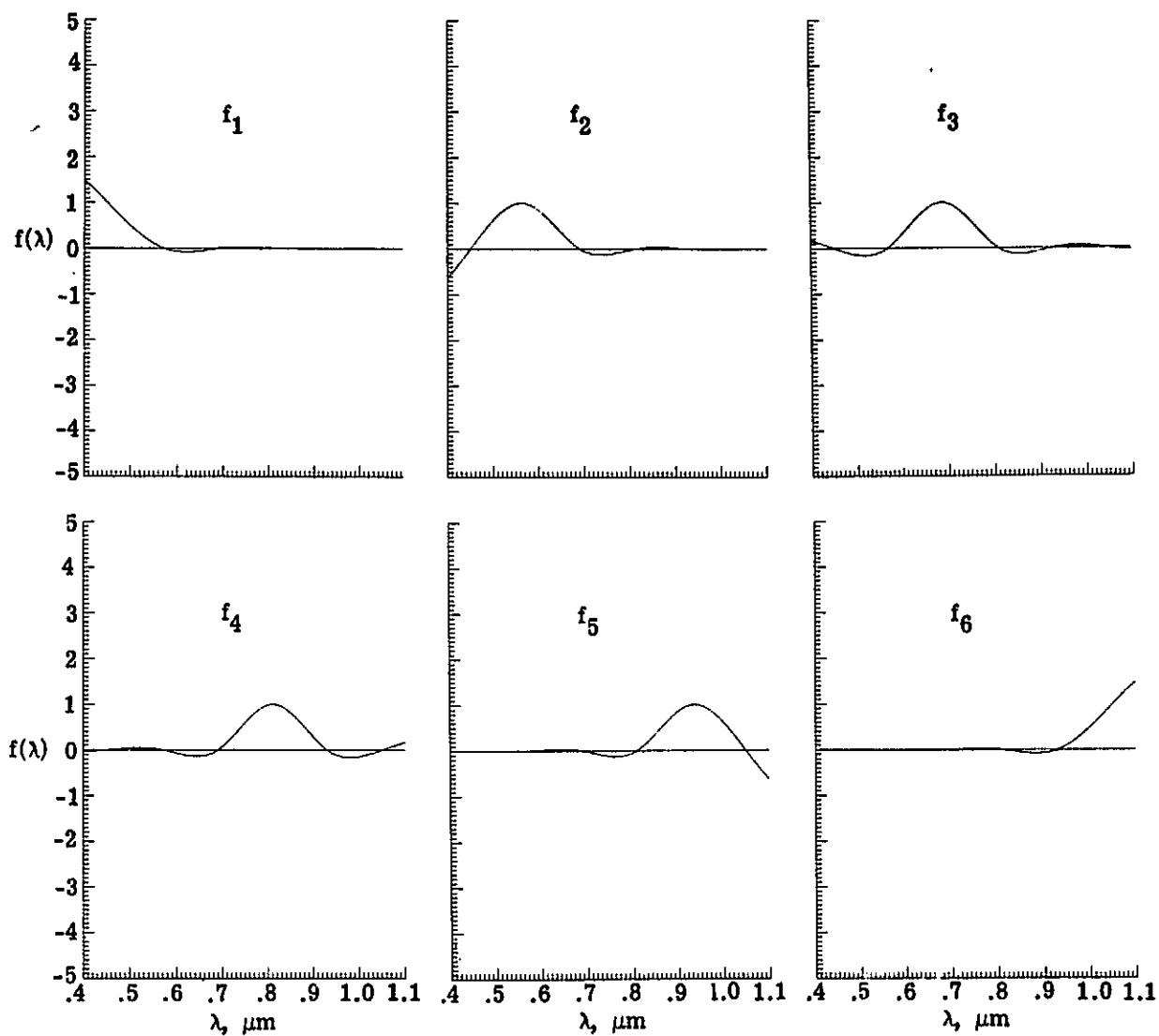
Figure 20.- System characteristic functions for an idealized system with
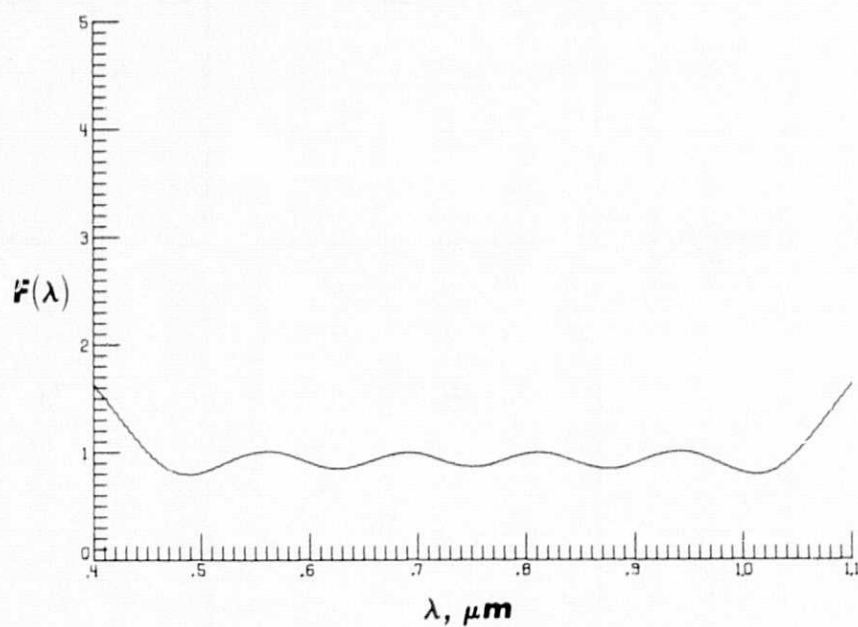impulse system transfer functions.

Figure 21.- Relative standard deviation of the reflectance estimates for an idealized system with impulse system transfer functions.